HYDROFOIL DESIGN & OPTIMIZATION FOR FAST SHIPS

by

**Eric Besnard, Adeline Schmitz, George Tzong,
Kalle Kaups, Hamid Hefazi, John Hess
Hsun Chen, and Tuncer Cebeci**

**Aerospace Engineering Department,
California State University, Long Beach
Long Beach, CA 90840**

19980303 092

REPORT AE–98-1

DTIC QUALITY INSPECTED 3

January 1998

TABLE OF CONTENTS

C S U L B Foundation

February 26, 1998

Attn.: Administrative Contracting Officer
Office of Naval Research
Regional Office San Diego
4520 Executive Drive, Suite 300
San Diego, CA 92121-3019

Re: Grant # N00014-97-1-0964

Administrative Contracting Officer:

Enclosed please find the one copy of the Final Technical Report, the Final Request for
Reimbursement (SF 270), the Final Financial Status Report (SF 269), and the Final Patent
Report (DD 882) for the above referenced program. If you have any questions, please don't
hesitate to contact me at 562-985-5233.

Thank you for your support of this research.

Sincerely,

Sandra A. Shereman
Director, Grants & Contracts

Enc. 4

SAS/bem

DTIC QUALITY INSPECTED 3

cc: Foundation Archive
        G&C File #07-176097

LIST OF FIGURES

LIST OF TABLES

NOMENCLATURE

M: mass (tons)

V: speed

ρ: sea water density ($\rho = 1030$ kg/m^3)

D: drag force $\left(D \equiv D_i + D_f + D_s \right)$

L: lift force

p_V: vapor pressure

S: reference area (foil area)

d: depth (m)

b: span (m)

c: chord (m)

$<t/c>$:   average maximum thickness ratio

t/c: maximum thickness ratio

η: normalized spanwise coordinate $\left(\eta \equiv y/b \right)$

A: aspect ratio $\left(A \equiv b^2/S \right)$

σ_i: cavitation index $\left(\sigma_i \equiv \left(p_\infty - p_V \right) / \left(\tfrac{1}{2} \rho V^2 \right) \right)$

λ: sweep angle

α: angle of attack ($^\circ$)

η_p: propulsive efficiency

c_ℓ: section lift coefficient

c_d: section drag coefficient

C_L: total lift coefficient $\left(C_L \equiv L / \left(\tfrac{1}{2} \rho V^2 S \right) \right)$

C_D: total drag coefficient $\left(C_D \equiv D / \left(\tfrac{1}{2} \rho V^2 S \right) = C_{Di} + C_{Df} + C_{Ds} \right)$

C_{Di}:   induced drag coefficient $\left(C_{Di} \equiv C_L^2 / (\pi A e) \right)$

$C_{Df,s}$:   profile drag coefficient of foil or strut

e: efficiency factor (see induced drag)

C_p: pressure coefficient $\left(C_p \equiv \left(p - p_\infty \right) / \left(\tfrac{1}{2} \rho V^2 \right) \right)$

c_f: local skin friction coefficient

C_f: total skin friction coefficient

R_C: chord Reynolds number $\left(R_C \equiv Vc/\nu \right)$

n_s: number of struts

Subscripts

$\cdot_f$:   foil

$\cdot_s$:   strut

1.0 INTRODUCTION

This report was prepared in response to an ONR request to evaluate computationally hydrofoil based fast ship concepts. The specifications for this study were formulated to drastically reduce sea lift transit times to remote locations by a factor of five when compared to the present drag speeds of 20 knots for the upper limit of the desired speed of 100 knots. Typical projected minimum destinations and transit times are shown in Fig.1.1. Because this study was commissioned to concentrate on a single lifting surface carrying up to 10,000 metric tons of mass above the sea surface no judgment was made as to the number and arrangement of separate foils necessary for a realistic configuration. Likewise, the analysis is for a smooth sea surface and free of assumptions regarding stability and control or the problems of propulsion. To aid in the visualization of the concept in action a possible configuration, as seen through the eyes of an artist is shown in Fig. 1.2.
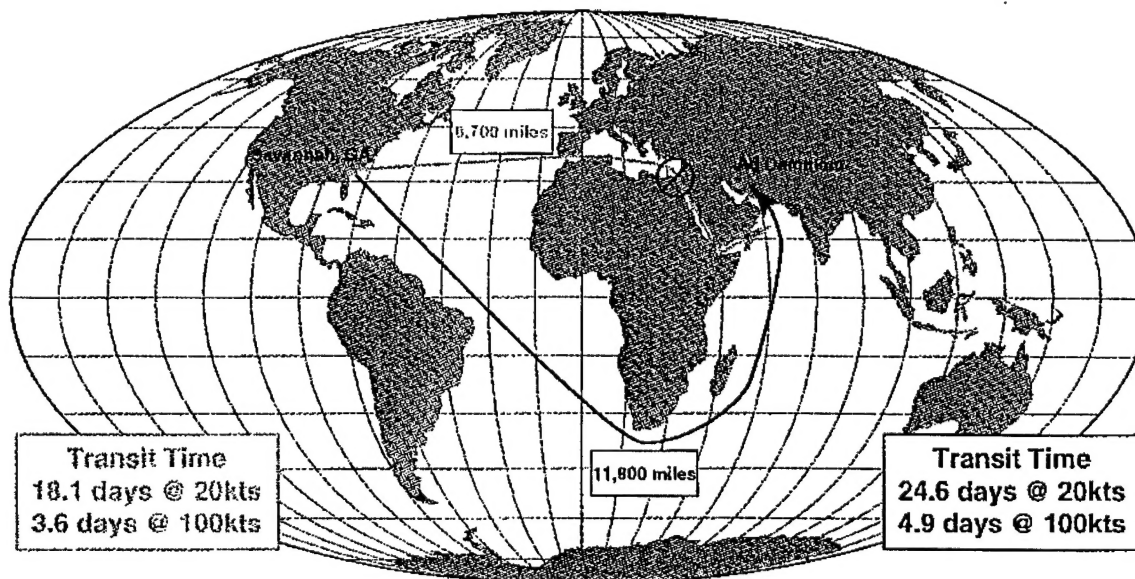
Fig. 1.1 Typical projected minimum destinations and transit time
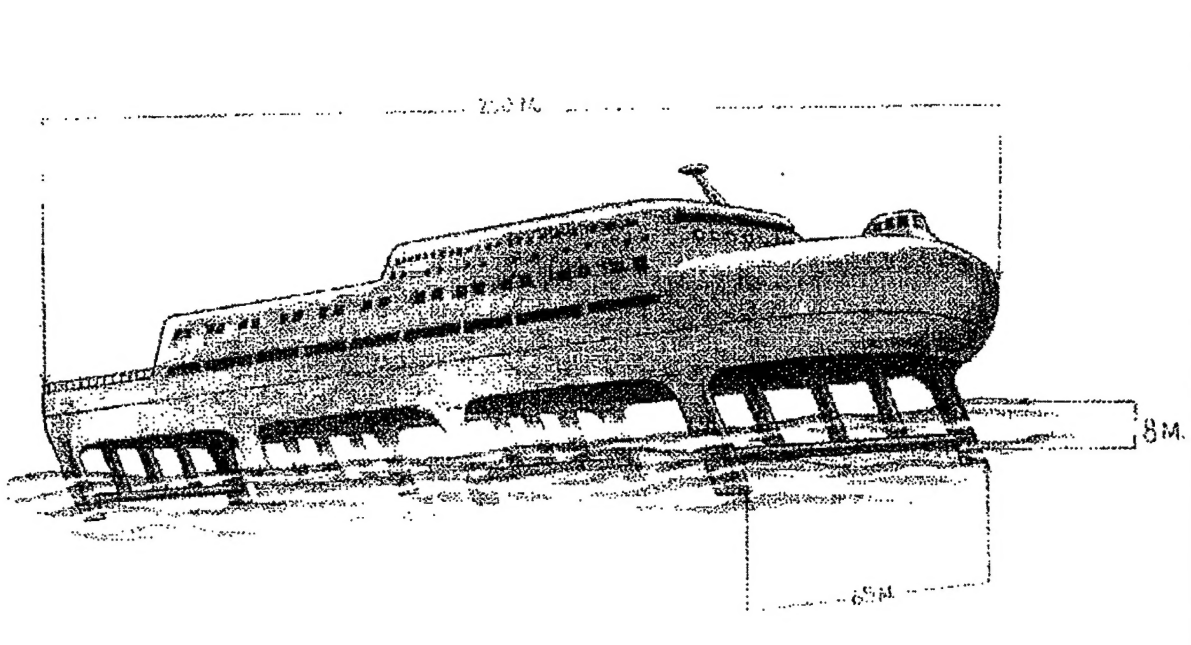
Fig. 1.2 Artist concept of fast ship

The basic requirement, and the essential factor in attaining a range of at least 10,000 nautical miles, was the determination of the maximum practical lift to drag ratio, L/D consistent with the desired high speed, limits set by cavitation onset and structural considerations. With respect to the maximum L/D it should be noted that the calculated L/D values are not the classical maximum L/D values of the induced and profile drag coefficients because cavitation onset severely limits the maximum lift coefficient available. A corollary to this is that in the Breguet range formula the L/D value to be used is the one obtained under the restricted condition and not the theoretical maximum. Another point regarding the use of the range formula is that for the present case in order to operate at constant L/D requires a speed change as the fuel is burned. The alternative is to operate at constant speed but at variable foil incidence oor L/D during the voyage.

Since the minimum drag for a given lift coefficient depends on the number of struts prescribed by structural consideration and because the lift coefficient determines the maximum foil thickness possible, there is strong coupling between structural strength and the

2

cavitation number. To evaluate structural requirements and their effect on drag all configurations in this study were analyzed by the finite element method.

In keeping with the preliminary nature of this study most configurations analyzed had a rectangular planform with foils of constant thickness and uniform cross-section with support struts having the same chords as the foils. Recognizing that the cavitation onset criterion, subject to structural constraints, is the main contributor to the hydrodynamic performance, the basic problem then was to analyze each configuration for a assumed set of weight, speed and operating depth below the free surface by varying the foil aspect ratio and foil thickness. Since the object was to obtain minimum drag and maximum lift with no cavitation or separation of the flow, iterations were necessary by varying design parameters because the number of struts is not known a priory.

The description of the work accomplished starts with the diagram overview which is essentially an outline of milestones for different tasks and objectives. This is followed by a chapter describing the computational tools used and the modification introduced in order to make them suitable for this particular application. The Hess panel code required extensive modifications to make it applicable to the free surface problem and the associated induced drag calculation. Correctness of these modifications was verified by running several test cases in comparison with known solutions and expected trends. To speed up the computational process an automatic paneling of the foil-strut or endplate configuration was incorporated. This allowed for a rapid variation of the geometry, a very useful feature for the generation of strut extension or endplate size perturbations. A separate chapter covers the optimization process for foil cross-sections. Since the spanwise lift distribution on a box-wing or foil is nearly constant a two-dimensional analysis was deemed sufficient for the preliminary evaluation purpose. It boils down to finding the maximum lift and minimum drag for the selected cavitation number, speed, and foil maximum thickness ratio. In principle the sectional analysis could be applied at separate spanwise stations if the local lift coefficient is known although the iteration procedure must be revised. Similar optimization may be applied to the strut drag but the matter is complicated by venting to the atmosphere. It should be

added that the foil or strut section viscous drag calculations are based on the interactive boundary-layer solutions over the foil surface and extended into the wake where the total drag is determined from the momentum loss in the far field. The skin-friction contribution is obtained by integration of the wall shear stress over the foil surface.

The subchapter on structural analysis outlines the details of the finite element analysis, the basic assumptions, and its use in the foil-strut problem. Critical areas of the structure are identified, where foil bending dominates. It is pointed out that the selection of the allowable stress level has an effect on the outcome in terms of the number of struts required. There is also a discussion on alleviating high stresses by local reinforcements which may at the same time be effective in reducing the hydrodynamic interference at the foil-strut intersection for example.

There is a whole chapter on the design approach which is an elaboration of how the separate parts fit together and influence each other. The reader should note that besides the lengthy and fully iterated optimization procedure outlined several short cuts or cross-overs are possible and are used in the preliminary analysis to obtain many reasonable estimates instead of a few accurate solutions within the limited timeframe.

The last two chapters present the calculated results, one covers the single foil configurations and the other biplane configurations which were included to explore ways to shore up the structural rigidity in order to reduce the number of struts. Most of the analysis presented is at the minimum desired speed of 75 kts and mass of 5000 metric tons with a few excursions to speeds of 60 kts and 90 kts. The effect of weight on performance is demonstrated by calculations at 10,000 metric ton weight and 75 kts speed. The foil operating depth range considered varied from 10 m to 20 m. It should be repeated that the presented relatively low maximum lift coefficients are entirely due to the limitations imposed by the specification of a cavitation free flow. This in turn results in large wetted surface area and high profile drag in order to carry the required mass. Additional profile drag is contributed by the struts which are designed according to structural requirements. Summary data tables also

contain information on L/D-values obtainable if the computed profile drag is reduced to a half or a quarter of its original value. An alternative interpretation of the profile drag reduction is the effect on drag when some struts are eliminated.

The report concludes with a summary of results and a discussion of the achievable L/D values, power requirements and possible avenues for improvements.

2.0 PROGRAM OVERVIEW

The program overview is presented in Fig. 2.1. The design of hydrofoil ships cruising at high transit speeds (50 - 100 knots) and capable of sustaining these speeds for long unrefueled legs (> 5000 Nmi) requires minimizing drag while generating the prescribed lift and without violating any other constraints (e.g. span < 65 m). Many areas of engineering such as hydrodynamics and structure play a key role and are closely tied to the design. Before attempting to design the hydrofoil system, care must be taken to ensure that the proper tools are used.

Therefore, the first phase of the project (July - Sept. 1997) consisted of obtaining or developing the *necessary tools*:

1. **Panel method with free surface modeled by negative image**. The method is described in detail in Sect. 3.1 and is used to compute three-dimensional flows about arbitrary configurations in order to determine the pressure, lift, and induced drag coefficients. A computer program was also developed to panel automatically the various foil-strut configurations. Applications of the programs are presented in Sect. 3.1.

2. **Foil cross-section optimization tool**. This tool is described in Sect. 3.2 and is composed of an optimizer, a code which represents general foil shapes by a set of design variables, and a validated Computation Fluid Dynamics code. The optimization tool is used to design foil cross-sections which, for a given maximum thickness, produce the highest lift coefficient possible without causing any cavitation and flow separation. The profile drag is calculated in the CFD block of the tool. Applications are also shown in Sect. 3.2.

3. **Structural analysis tools**. The foil-strut system is subject to vertical, drag, and side loads, and the structural analysis can be appropriately performed by using the Finite Element method. As explained in Sect. 3.4, this analysis needs to be conducted numerous times. In order to expedite the Finite Element model generation, a computer program was developed. This program, given a set of

structural design variables, generates the model automatically and prepares the input data for the Finite Element analysis. Details are described in Sect. 3.4.

In parallel to the tool development, a ***design approach*** using these tools was developed. Given a transit speed and a mass to lift, a design process and the corresponding independent design variables were identified. The design approach is presented in Sect. 4.0.

During the next phase (Sept. 97), ***preliminary L/D calculations*** were carried out for a *single foil configuration* to identify the ***key parameters*** driving the design and getting lower bounds on achievable L/D values. Following these preliminary calculations, several modifications to the design were implemented to identify areas which could lead to significant improvements. Local structural reinforcements were one of these design considerations yielding improvements in L/D and were incorporated in the subsequent designs. The results obtained during this phase are described in Sect. 5.0.

A *biplane configuration* was also analyzed in order to determine the potential of using other types of configurations to possibly reduce the number of struts required and thus improve L/D. Results are presented in Sect. 6.0.

Finally, a limited number of test cases were analyzed by ***varying the design parameters*** over the design space to capture the dependency of L/D on these variables. Results are presented in Sect. 5.0 for the single foil configuration and in Sect. 6.0 for the biplane configuration.
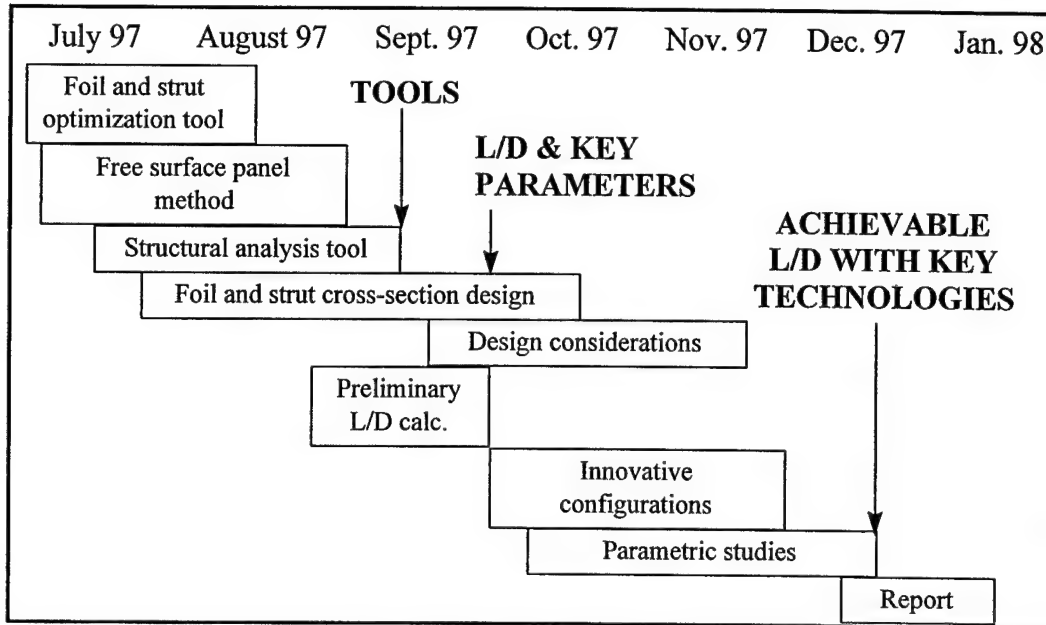
Fig. 2.1. Program overview

3.0 TOOLS

This chapter presents the tools necessary for the study. The calculation method used for three-dimensional flow calculations with the free surface modeled by negative image is presented in Sect. 3.1 along with sample test cases. Then, the design of foil and strut cross-sections is presented in Sect. 3.2 and 3.3, respectively. Finally, the tools and hypothesis used for structural analysis are presented in Sect. 3.4.

3.1 Three-dimensional flow computation and induced drag calculation

Hess panel method

The Hess Panel Method was first introduced more than thirty years ago (Ref. 1) and has been refined and extended over the years (Ref. 2 & 3) to make it more efficient and more generally applicable. Because of their robustness and simplicity, panel methods are well established as the methods of choice for analyzing low-speed flows about general three-dimensional configurations. While there are other panel methods in the literature, only the Hess version has been developed into a truly higher order version (Ref. 3), which is not only more accurate, but eliminates certain anomalies associated with earlier first-order formulations.

Because it is so well known, and indeed forms a standard chapter in all current fluid dynamics textbooks, a detailed description of a panel method seems unnecessary. Instead, a brief description of its principal features will be outlined. Fig. 3.1 illustrates the panel method analysis of the typical problem of three-dimensional lifting flow. The configuration consists of a non-lifting portion (e.g. a fuselage) and a lifting portion (e.g. a wing). A lifting portion is characterized by having a trailing edge from which issues a trailing vortex wake and along which a Kutta condition is applied. The non-lifting portion has no trailing edge and no wake. The complete configuration, both lifting and non-lifting portions as well as the wake, is discretized for the computer as a set of quadrilateral surface panels. Over these panels are distributed source and dipole/vorticity distributions, whose strengths are adjusted to satisfy

the boundary conditions. (The equivalence of dipole and vorticity distributions is proven in the report form of Ref. 2). In the Hess panel method, panels on the non-lifting portion have source singularity, wake panels have vorticity, and panels on the lifting portions have both. In addition there may be vorticity panels interior to the configuration to obtain more favorable numerics.
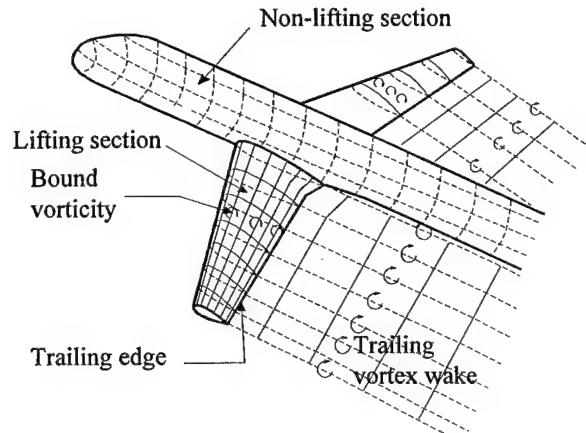
Fig. 3.1. Typical lifting configuration

The two main computational tasks of the panel method are; (1) compute the large full matrix of mutual panel influences and (2) solve a system of simultaneous linear equations for the singularity strengths. When these have been accomplished fluid velocities and pressures may be calculated both on and off the body. This technique has been used routinely over the years to obtain satisfactory design information in literally tens of thousand of cases. A typical application is given in Fig. 3.2, which shows a MD-90 in criuse configuration represented by 6900 panels on either side of the symmetry plane.
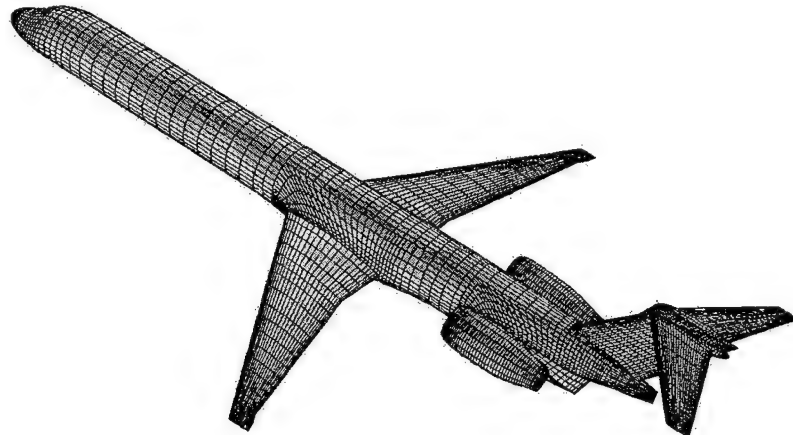
Fig. 3.2. MD-90 in cruise configuration

Induced drag calculation

The fundamental theorems of potential flow state that in three-dimensional cases a body cannot be lifting unless it sheds a vortex wake of the kind illustrated in Fig. 3.1. The wake represents energy imparted to the fluid, which implies a corresponding drag on the body, even in inviscid flow. Since this drag is present only because of the lift, it is often designated drag-due-to-lift or induced drag. The drag may be evaluated by calculating the energy in the wake by a far-wake procedure known as Treffez-plane analysis. Alternatively the calculated pressures may be integrated over the body panels to give the component of force in the free stream direction. In the limit of a large number of panels these two approaches converge to the same drag. It turns out that the Treffez-plane analysis approaches its asymptotic value more rapidly with panel number than the pressure integration. In past years, when panel numbers were restricted, the former approach was preferred. Now with more powerful computers either may be used. The agreement between the drags computed by the two procedures is a measure of the accuracy of the calculations.

Free surface modeling: introduction of negative image in Hess panel method

If a free surface is present as depicted in Fig. 3.3, in addition to the free-air conditions, the flow must satisfy a condition of zero (atmospheric) pressure along the free surface. The location is initially unknown. However, if disturbances are assumed small, i.e. velocity is not very different from its free stream value V and free surface height and slopes are small, the free surface condition may be linearized to

$$V^2 \phi_{xx} + g\phi_z = 0 \quad \text{on} \quad z = 0 \tag{3.1}$$

where g is the acceleration of gravity, condition (3.1) may be applied to either the total potential or the perturbation potential, since the free stream potential $\Phi_\infty = Vx$ gives zero when put in the left side of (3.1).
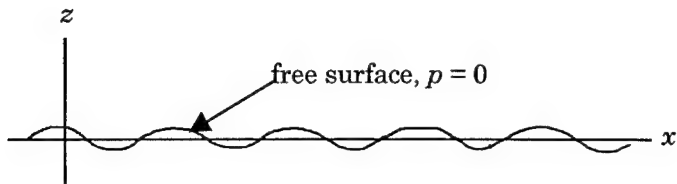
Fig. 3.3. Free surface flow

The incorporation of (3.1) into the problem is very difficult in general, but is easy in two limiting cases.

- *Case 1: Small V, low Froude Number*

  The first term in (3.1) may be neglected giving

  $$\phi_z = 0 \quad \text{on} \quad z = 0 \tag{3.2}$$

  i.e. $z = 0$ may be replaced by a solid wall.

- *Case 2: Large V, high Froude Number*

  The term ϕ_{xx} must be small or approximately

  $$\phi_{xx} = 0, \quad u = V \quad \text{on} \quad z = 0 \tag{3.3}$$

  where u is the velocity component in the free stream direction.

As is well known, Case 1 may be simulated by calculating the flow about the body and its mirror image in the $z = 0$ plane (positive image). In terms of sources and vortices, this means that any source or source distribution on the actual body gives rise to an equal source at the image point. A vortex, however, gives rise to a negative vortex at the image point. It is readily verified, that these combinations, shown in Fig. 3.4, give zero vertical velocity on $z = 0$.
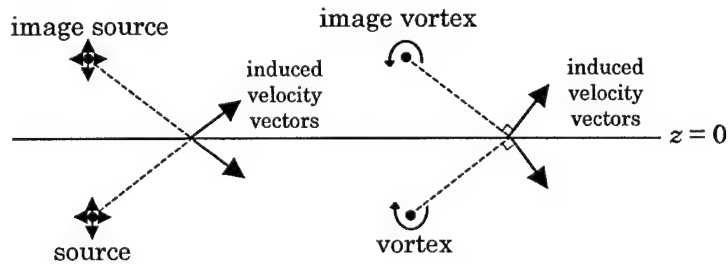
Fig. 3.4. Induced velocities with positive image.

Case 2 is less familiar. However, it turns out that, as shown in Fig. 3.5, the signs of the image singularities are reversed (negative image). It can be seen that these combinations

give zero horizontal velocity on $z = 0$, leaving the velocity there equal to free stream.
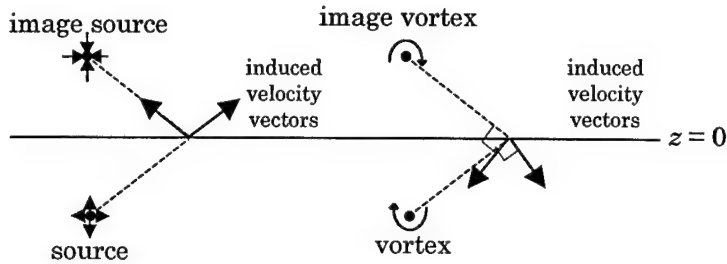
Fig. 3.5. Induced velocities with negative image.

The current version of the panel method includes options for either positive symmetry (solid boundary) or negative symmetry (free surface) on either the $y = 0$ or the $z = 0$ planes. The negative symmetry option was implemented during the course of the present study. In addition, combinations of two symmetry boundary conditions can be specified. For most of the test cases included in this report, a positive symmetry condition on $y = 0$ is combined with a negative symmetry condition at $z = 0$ to represent the water surface.

Test cases

Several test cases were run to ensure that the negative image option was properly implemented. In all cases considered, it was verified that the velocity component along the *x*-axis was equal to the free stream velocity in the $z = 0$ plane, i.e. the perturbation velocity is zero in that plane. Two sample test cases are presented in greater detail below. For both test cases, the foil has a constant chord $c = 3.59$ m, a span $b = 61.04$ m, and is placed at a depth d = 13 m. The foil has a cross-section designed to operate cavitation free at 75 knots with 8% maximum thickness and the strut has a thickness ratio of 0.08. This configuration corresponds to the test case S-3 which will be treated in detail in Sect. 5.

The first configuration considered has the strut chord equal to the foil chord and the strut does not extend below the foil (U-shape). Fig. 3.6 shows the corresponding variation of the load. In Fig. 3.6 (and Fig. 3.8), C_n is the normal force coefficient, c the local chord and $\bar{c}$ the average foil chord. The load on the foil is almost constant up to the junction. It is continuously transferred to the strut, drastically diminishes when getting closer to the surface,

and goes to zero in the plane of negative symmetry. Fig. 3.7 presents the velocity vectors in the junction region and shows that the flow is well behaved and properly computed in that region.
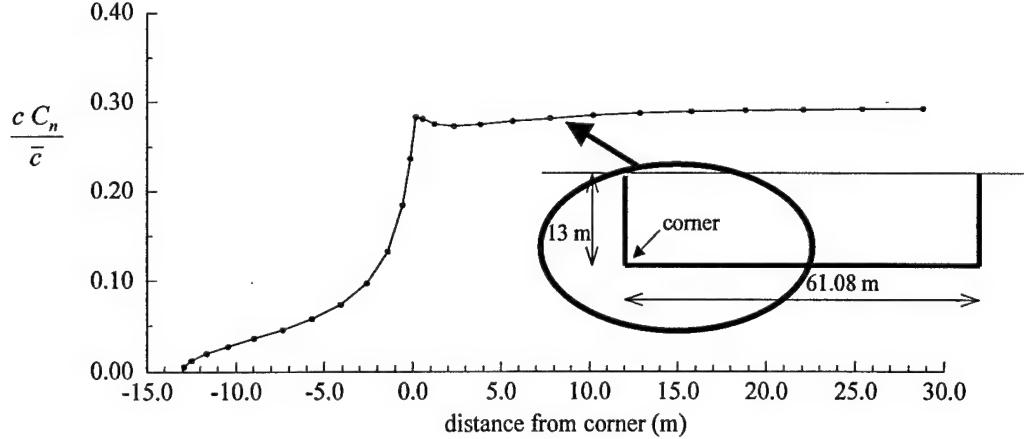
Fig. 3.6. Load variation for the U-shape foil-strut configuration.
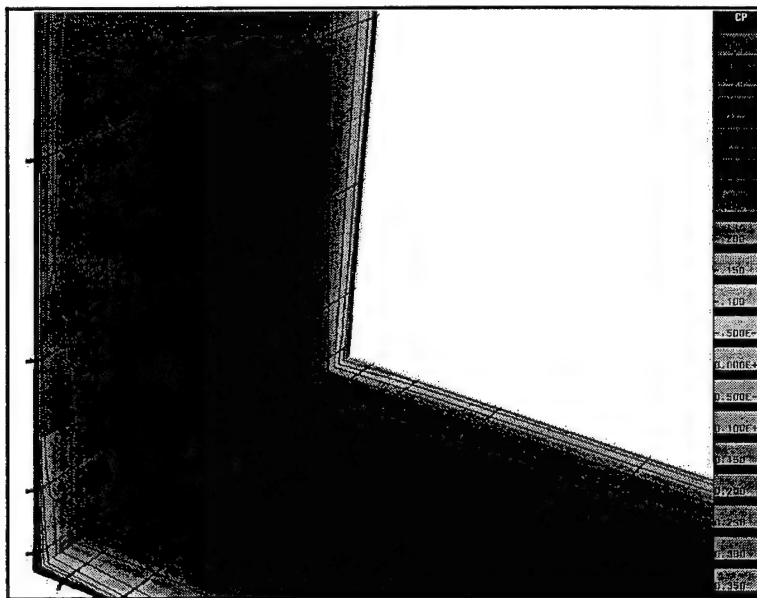
Fig. 3.7. Velocity vectors and pressure contours in the neighborhood of the foil-strut junction for the U-shape foil-strut configuration.

The continuity of the total load at the junction for the case of an endplate (H-shape) is shown by slightly increasing the chord of the strut and extending it below the foil. The dimensions of the strut are shown in Fig. 3.8 along with the corresponding load distributions. It is seen that the load of the foil is transferred to both upper and lower parts of the end-strut. Fig. 3.9 presents the corresponding velocity vectors near the junction.
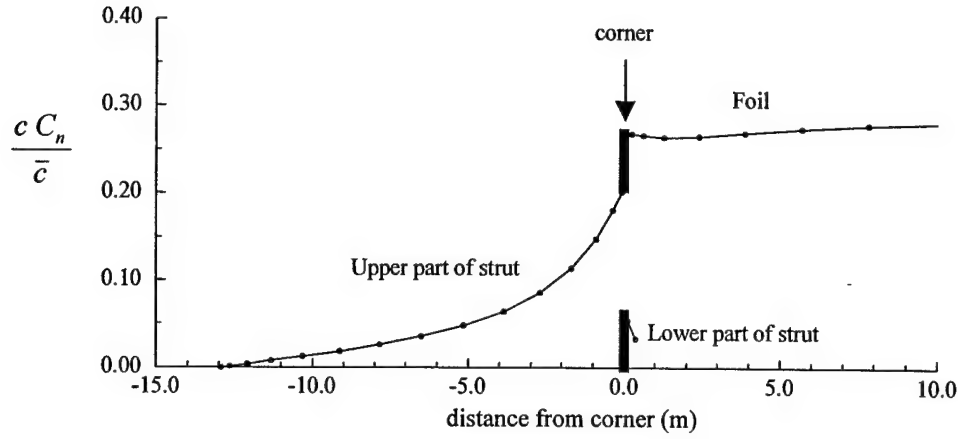
Fig. 3.8. Load variation for the H-shape foil-strut configuration.
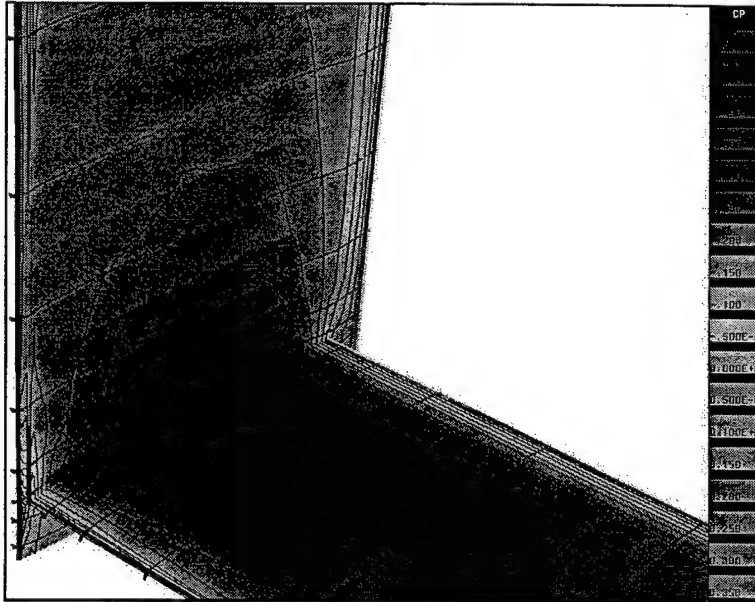
Fig. 3.9. Velocity vectors and pressure contours in the neighborhood of the foil-strut junction for the H-shape foil-strut configuration.

Effect of end-struts and free surface (negative image) on induced drag

For a single wing without winglets in free air, or equivalently at infinite depth in water, the optimum load distribution is elliptic and the corresponding induced drag coefficient is given by

$$C_{Di} = \frac{C_L^2}{\pi A e} \tag{3.3}$$

with $e = 1$.

15

The induced drag can be reduced by adding winglets. For hydrofoil applications, struts linking the foil to the boat hull need to be employed, and if the structural requirements imply a "large" number of struts, say greater or equal to 3, it might be beneficial to use these struts as winglets. Fig. 3.10 shows the benefit of adding end-struts to a foil with a rectangular planform. When no end-struts are used, the efficiency factor for the rectangular foil is, as expected, slightly less than 1. With relatively small end-struts, the efficiency factor rapidly increases to values greater than 1.
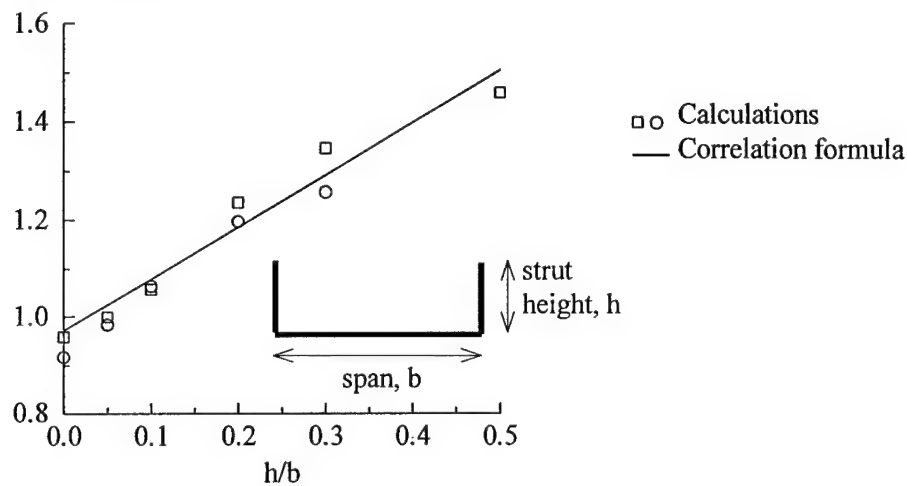
Fig. 3.10. Efficiency factor, e, for foil / end-strut configuration at infinite depth.

The other benefit of using end-struts is the modification of span loading. Fig. 3.11 shows the span loading for a rectangular wing with and without end-struts and illustrates how the use of struts enables to increase the lift coefficient. This is of particular interest for minimizing total drag, for it allows to have a smaller wing generating the same lift.
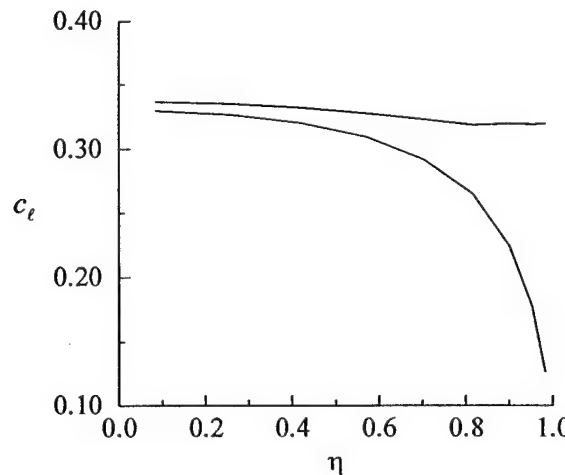
Fig. 3.11. Effect of end-struts on the span loading of a rectangular foil.

The benefits of having end-struts remain in the presence of a negative image (to model the free surface). The induced drag, however, is drastically increased, as depicted in Fig. 3.12. For example, struts with $d/b = 0.3$ are required to reach an efficiency factor corresponding to elliptic loading ($e = 1$).
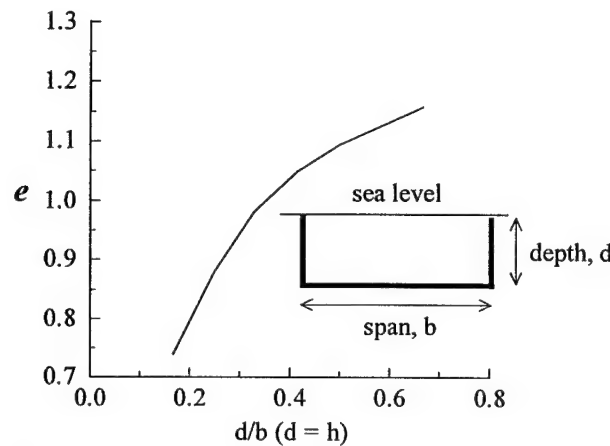
Fig. 3.12. Efficiency factor, e, for foil / end-strut configuration at finite depth.

3.2 Hydrofoil cross-section optimization and profile drag calculation

3.2.1 Design Optimization method

Conventional airfoils cannot be used for underwater high speed applications because of cavitation. If the pressure on the upper surface of the airfoil reaches vapor pressure, intermittent air bubbles form and erode the foil surface very rapidly. So far, no material as been found that can resist cavitation for a long period of time. Also, cavitation induces more drag which is opposite of what is being seeked. It is therefore necessary to design a cavitation-free foil. Cavitation inception depends on the speed and depth at which the foil is operating. Cavitation occurs when the local $C_p = -\sigma_i$, where σ_i is the cavitation index.

$$\sigma_i = \frac{P_{stat}}{q} = \frac{P_{atm} + \rho g d - P_v}{\frac{1}{2}\rho V^2} \tag{3.4}$$

Thus, hydrodynamic problems introduce a constraint on the pressure distribution because of cavitation. A family of cavitation-free profiles that maximize lift (thus minimizing the required lifting wetted area) for the cavitation indexes corresponding to various combinations of speed and depth possible needs to be designed. For a given cavitation number, there is an infinite number of profiles that are cavitation free with the thinner ones leading to higher lift and lower drag coefficients. Unfortunately, the structural strength of the configuration depends directly on the foil thickness and thickness variations must be considered.

Therefore, a two-dimensional optimization was implemented to find the "best" cavitation-free profile (maximum lift) for a certain maximum thickness to chord ratio (t/c). For a chosen σ_i, this allows to determine at which two-dimensional lift coefficient a foil with a given t/c can operate and calculate the resulting drag (friction + form). Also the foil is designed so that there is no flow separation, which would otherwise greatly increase the drag.

A general optimization process is illustrated in Fig. 3.13. An initial set of s design

variables, $\mathbf{x} = (x_i)_{1 \leq i \leq s}$, which might represent the configuration designed by experienced engineers, is supplied to the optimizer. Then, for this design, the objective function, f, is evaluated and the constraints, g_i, are analyzed to check whether they are violated or not. If the optimum is not reached, these values are fed back to the optimizer that modifies the design vector $\mathbf{x}$. The process is repeated until convergence.

For the application to aerodynamic or hydrodynamic optimization, the three main components of the numerical method are, (1) the representation of a configuration by a set of design variables, $\mathbf{x}$, (2) the optimization method, and (3) the evaluation of the aerodynamic or hydrodynamic performance, i.e. f, for a given configuration. The constraints g_i are analyzed at the stage appropriate for the problem considered.
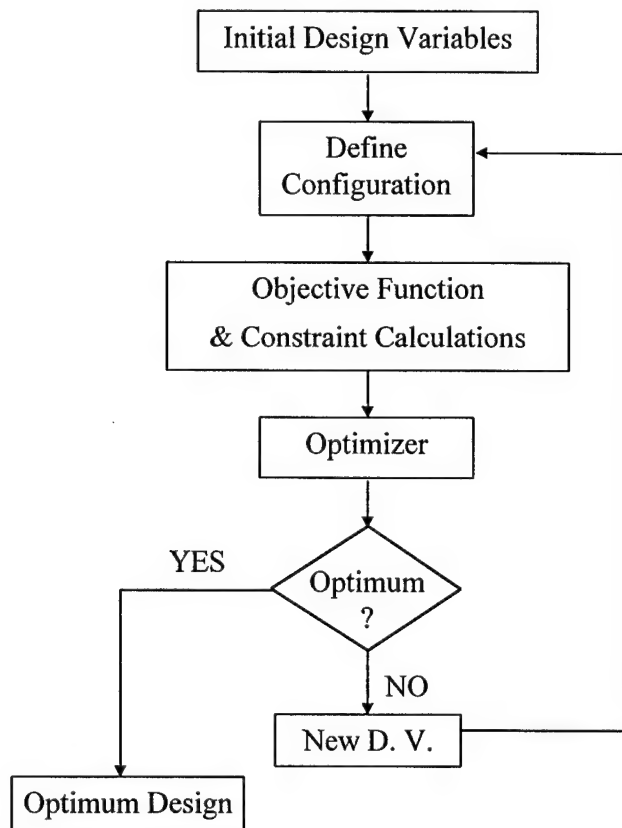
Fig. 3.13. Flowchart of the numerical optimization.

For the present problem, the design variables are shape function coefficients described below which represent the foil geometry. The objective function is the lift coefficient

calculated using an Interactive Boundary Layer approach discussed in the present section. The constraints are:

$$\begin{cases} -C_{p_{\min}} \leq \sigma_i & \text{:cavitation} \\ c_f > 0.0 & \text{:skin friction} \\ (t/c)_{\max} \text{ given} & \text{:foil thickness ratio.} \end{cases}$$

Optimizer

In the present study, the optimizer used is a commercially available optimizer DOT (Ref. 4), based on the method of Modified Feasible Directions (MFD). One optimization iteration consists of first determining a "Search Direction" which defines how the design variables will be changed. The search direction depends on the gradients of the objective function and of the constraints, if any. In the present study, all gradients are calculated by finite difference. The second step, called "One-Dimensional Search", is to determine how far to move in that direction.

Design variables to represent airfoils

To perform the optimization, one must be able to represent a general shape by a set of functions. Upper and lower surfaces of an airfoil can be represented by

$$y(\overline{x}) = y_0(\overline{x}) + \sum_{i=1}^{s} x_i\, f_i(\overline{x}) \tag{3.5}$$

where $\overline{x}$ is the coordinate along the airfoil chord, y_0 is a reference airfoil, e.g. a NACA 0012 airfoil, $(x_i)_{1 \leq i \leq s}$ are the design variables and $(f_i)_{1 \leq i \leq s}$ are the base functions. Several types of base functions such as Hicks-Henne functions (Ref. 5), Wagner functions, Legendre and Patched Polynomials (Ref. 6), etc., can be used. Hicks-Henne functions are selected for the present application and are given by:

$$f_i(x) = x^a (1-x) e^{-bx}$$
$$f_j(x) = \sin\left(\pi x^{\frac{\ln(0.5)}{\ln(a)}} \right)^b \tag{3.6}$$

where a and b control the center and thickness of the perturbation, and x is the normalized coordinate along the chord. They have the advantage of being space based functions, as opposed to frequency based functions (like Wagner functions), and thus allow for greater local control of the design.

Interactive Boundary Layer (IBL) approach for performance predictions

For a given configuration, the flowfield can be calculated by either solving the Navier-Stokes (NS) equations or employing an Interactive Boundary Layer (IBL) approach, which is based on the interactive solution of the inviscid and boundary layer equations. While the latter is not as general as the former, it offers a good compromise between the efficiency and the accuracy needed in a design environment and is therefore selected here. Also, for the purpose of hydrofoil design subject to low cavitation numbers, Reynolds numbers are large, viscous effects are small and therefore the boundary layer approximation is appropriate. Thus for the present application, results with IBL are as accurate as with NS methods.

The IBL method has been used extensively for single and multi-element airfoil flowfield predictions and is described in greater detail in previous publications (Ref. 7). Its ingredients are shown in Fig. 3.14. The inviscid flow field is computed by a panel method. Once the external velocity distribution is known, the boundary layer equations are solved in an inverse mode using the Hilbert integral formulation to allow for the computation of possibly separated flows (Ref. 8). Transition is determined as part of the solution procedure, employing either the e^n-method or correlation formulas. Since for the present application all calculations are performed at very high Reynolds numbers, transition was set near the stagnation point for all calculations. The turbulent flow calculations employ a modified Cebeci-Smith eddy viscosity formulation validated for both accelerating and adverse pressure gradient flows (Ref. 9). The displacement thickness and blowing velocity distributions are used to simulate the viscous effects in the inviscid method. The procedure is repeated until convergence.

The two dimensional profile drag (friction + pressure) is calculated several chords downstream of the trailing edge with the Squire-Young formula (Ref. 10)

$$c_d = 2\overline{\theta u_e}^{\left(\frac{H+5}{2}\right)}$$
(3.7)

where $\overline{u_e} \equiv u_e/V$ is the velocity at the edge of the boundary layer normalized by the freestream velocity, $H \equiv \delta^*/\theta$ is the shape factor, δ^* is the displacement thickness, θ is the momentum thickness and $\overline{\theta} \equiv \theta/c$.

If the skin friction is reduced to ½ or ¼ of its nominal value, the pressure drag is also reduced to ½ and ¼, respectively. This means that the profile drag results can be divided by 2 or 4 to account for a reduced skin friction.
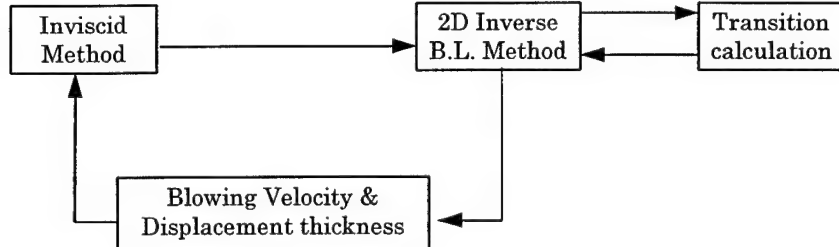
Fig. 3.14. Interactive Boundary Layer approach.

Validation of the IBL method

The IBL calculation method was applied and validated for numerous single and multi-element airfoils (Refs. 7, 11). A sample of results is shown here for the NACA0012 airfoil.

Fig. 3.15 shows the variation of the lift and drag coefficients of that airfoil for a chord Reynolds number of 3×10^6. Calculated results agree well with measurements (Ref. 12) up to stall. As can be seen, the measurements of drag coefficients do not extend beyond an angle of attack of 12 degrees but at lower angles of attack, the measured values agree well with the calculations. Note that the calculated lift-drag curve at higher angles of attack shows the expected increase in drag coefficient in conjunction with reduction in lift coefficient for post-

stall angles.

For hydrofoil applications, angles of incidence are small (less than 0.5°) and previous results show that, for these conditions, the calculation method is extremely accurate for both lift and drag coefficients.

(a)   (b)
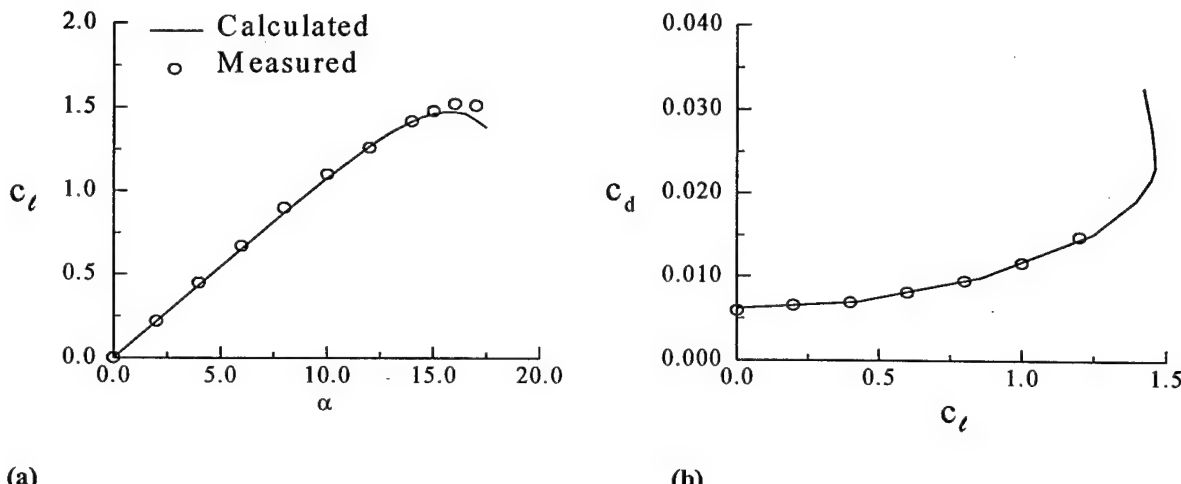
Fig. 3.15. Comparison between calculated and experimental values of: (a) lift coefficient and (b) drag coefficient for the NACA 0012 airfoil at $R_c = 3 \times 10^6$.

The design optimization approach has been successfully implemented for several high lift applications including inverse design (pressure matching), maximizing the maximum lift coefficient of an airfoil, and maximizing the L/D ratio of multi-element airfoils by adjusting their relative positioning (Ref. 11).

The next paragraph presents results obtained for hydrofoil design.

3.2.2 Application to hydrofoils for various cavitation indexes

As mentioned in Section 3.2.1, the IBL code is coupled with DOT optimizer to design foil profiles that maximize lift coefficient. The constraints for this application are multiple and are evaluated at different stages depending on the type of constraint considered. The cavitation

constraint imposes a minimum pressure on both lower and upper foil surfaces. The thickness constraint imposes a maximum thickness (calculated perpendicular to the foil chord) on the profile, limiting the design space. Then the no-separation criterion limits the local skin friction coefficient on the foil surface to a very small positive value to avoid a separation bubble and a resulting increase in drag.

Calculations have been made for cavitation numbers between 0.15 and 0.6 for different thickness ratios. Those two limits for the cavitation index correspond to 100 knots, 10 meters depth, and 50 knots, 10 meters depth, respectively. For each case there is a maximum t/c that can be reached corresponding to the appearance of cavitation on the lower surface of the foil. When the speed increases, or the depth diminishes, the maximum thickness achievable gets smaller. Fortunately, at 100 knots, 10 m the maximum thickness attainable is still around 5% which may be "reasonable" for the structural considerations.

Fig. 3.16 shows a sample of profiles and pressure distributions obtained for $\sigma_i = 0.267$ and various thickness ratios using the design optimization method of Sect. 3.2.1. The upper surface changes very little with increased thickness because the pressure distribution is limited by the no-cavitation criterion. Only the lower surface changes with the imposed t/c. For the thickest foil (t/c = 8.5%), the maximum negative pressure on the lower surface reaches values close to the cavitation index. Cavitation will occur on the lower surface for a slightly thicker profile.

Fig. 3.17 shows the lift and drag coefficients for the entire range of cavitation indexes studied and for two Reynolds numbers (60×10^6, 100×10^6). The drag coefficient depends very little on lift coefficient because the pressure distribution is very similar from one profile to another. Therefore, drag mostly depends on foil thickness and Reynolds number. Correlation laws have been derived to predict lift and drag coefficients as a function of thickness ratio, cavitation index, and Reynolds number and are represented by continuous lines in Fig.3.17.
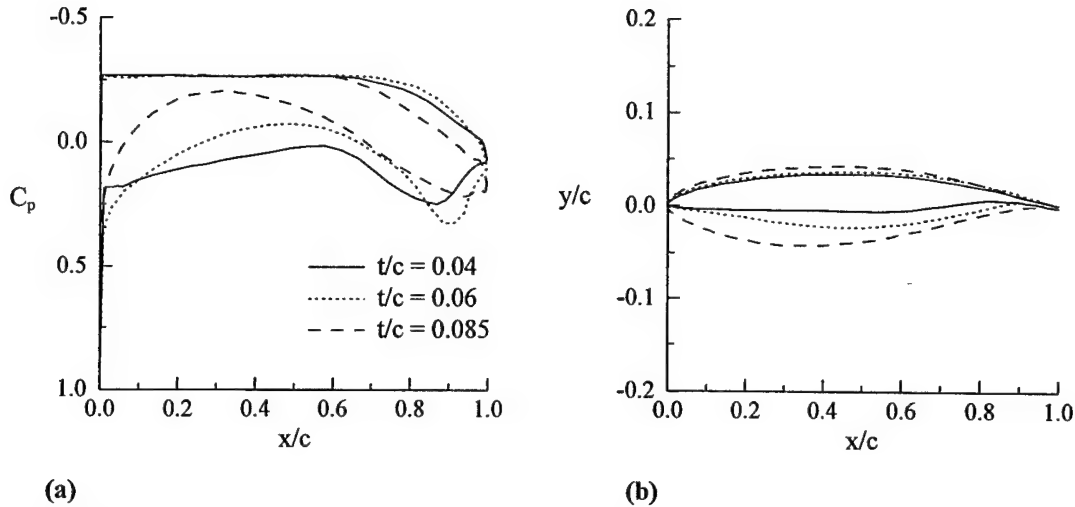
Fig. 3.16. Results of design/optimization for foil at $\sigma i = 0.267$; (a)Pressure distribution; (b) profile
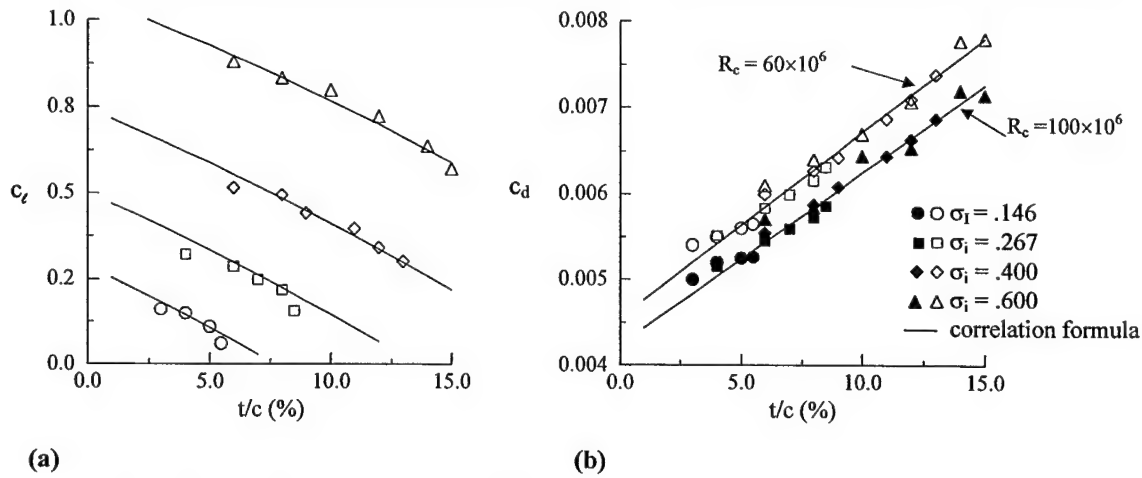
Fig. 3.17. (a) Lift and (b) drag coefficients for the entire range of cavitation indexes

Note that results are shown without free surface effects. For the depth to chord ratios considered, the presence of the free-surface slightly decreases the pressure coefficient on the foil upper surface. This effect being small and conservative, it has been ignored in the present calculations.

3.3 Struts profile drag calculation

Since the struts are non-lifting, the optimization should minimize the drag of a symmetric profile at zero degree angle of attack, with constraints of no-cavitation and fixed maximum thickness. For structural reasons the thickest possible profile should be chosen

25

since it has the highest bending strength.

Unfortunately, the cavitation index of the struts varies from the sea surface to the depth chosen for the foil. Therefore, the thickness ratio of the struts should vary from top to bottom. Also for the faster speeds (75 knots and over), the cavitation-free profile would become very thin near the sea surface. It might then be more advantageous to choose base vented struts or super-cavitating profiles. However, there are still too many unknowns and approximations to use a configuration detailing strut shape variations with depth in a feasibility study. Also as previously mentioned, profile drag is almost independent of the airfoil shape, it depends primarily on the thickness ratio and the chord Reynolds number.

Therefore, an existing family of symmetrical profiles was used to calculate strut drag as a function of R_c and t/c. The NACA 16-series airfoils have been chosen because they have a low peak maximum velocity, only slightly higher than ellipses ($v_{max} = 1 + t/c$). The family has approximately a linear variation of $v_{max}{}^2$ with t/c in the range $6\% \le t/c \le 16\%$. Since $\sigma_i = -C_p \equiv -1 + v_{max}{}^2$, σ_i will also be a linear function of t/c. Therefore, for a chosen cavitation index, the corresponding airfoil thickness is calculated and, using the NACA 16-series equations defined in Ref. 12, the airfoil ordinates are determined. The IBL code can then be used to calculate the profile drag coefficient. Fig 3.18 presents the strut profile and its pressure distribution for several cavitation numbers. It is expected that if drag were minimized using the optimization method used for foil design, the drag reductions compared to the NACA 16-series airfoils would be small, since pressure distribution and foil thickness would be very similar.

Fig 3.19a shows the variation of thickness ratio with cavitation index for the NACA 16-series struts. Fig. 3.19b presents the strut drag coefficients obtained for the struts for t/c varying from 6% to 16% and R_c of 60×10^6 and 100×10^6. Similarly to the foil, correlation laws can then be derived from Fig. 3.19 to predict the profile drag as a function of thickness ratio and Reynolds number. Also for this study, a cavitation index corresponding to mid-depth has

been chosen to estimate strut cross-section thickness ratio and drag coefficient.
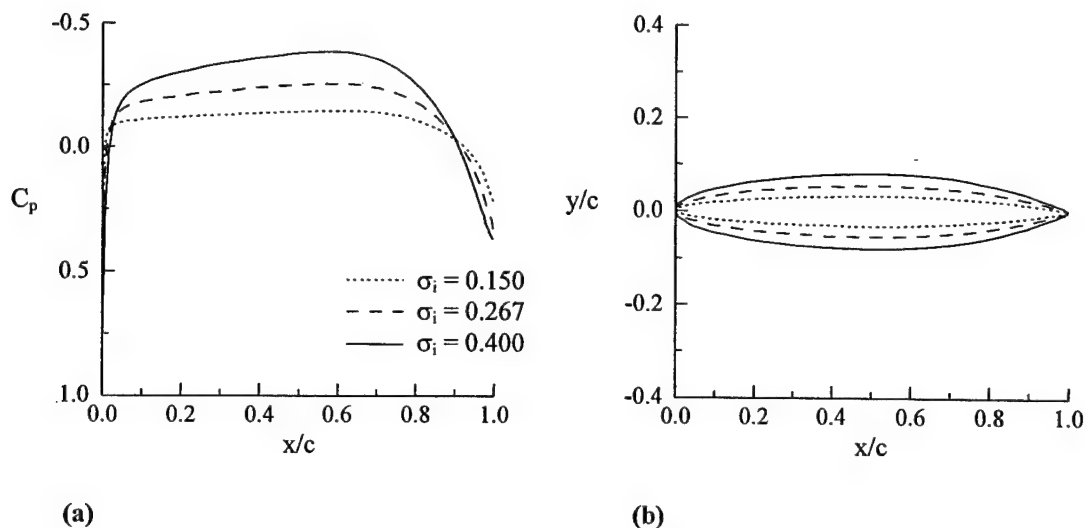
Fig. 3.18. (a) Pressure coefficient and (b) strut profile (NACA 16-series airfoil) for different cavitation indexes
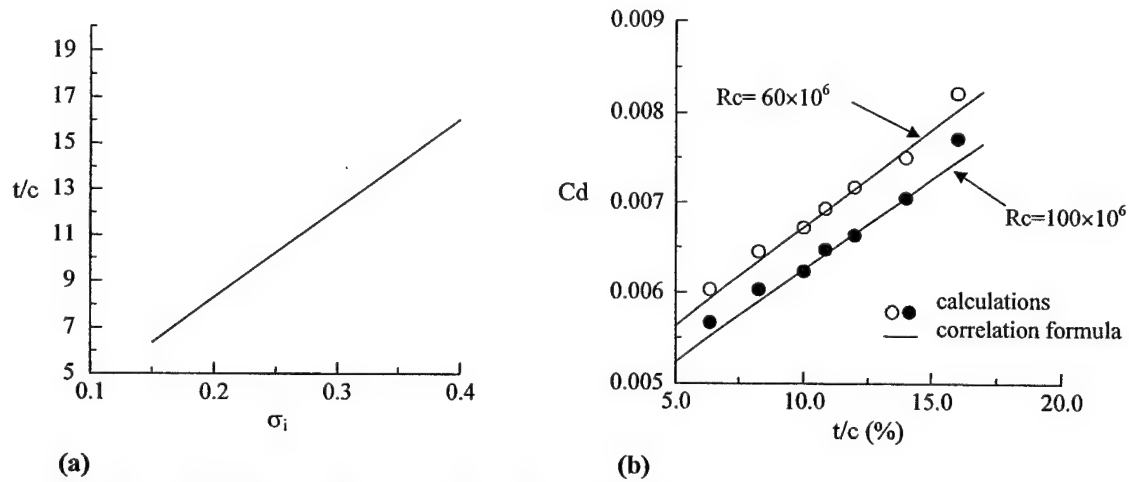
Fig. 3.19. (a) Thickness ratio in function of the cavitation index; (b) Drag results for NACA 16-series

3.4 Finite Element Structural Analysis

In the preliminary design phase, structural analysis is necessary to determine the layout of assembly of wing and struts that leads to the best performance of a fast ship. The struts introduce substantial drag forces to the ship. Hence, it is desireable to minimize the number and sizes of struts in order to improve the ship's performance, i.e., increase the L/D ratio. However, the struts must be sufficient to support critical design loads from ship weight, ocean waves and ship maneuvering. The wing needs to carry design payloads. If the wing foil is not strong enough, intermediate struts will be installed to reduce wing span between struts. Therefore, trade-offs among design parameters such as the number of struts, wing and strut foil dimensions and wing span need to be studied in order to optimize the ship's L/D ratio.

The configuration of wing and strut assembly is like a multi-bay frame with finite dimensions of foils as shown in Fig. 3.20. As described in Sect. 4, given the configuration lift coefficient, the foil area is calculated to lift the required load and from the selected aspect ratio, foil chord and span are derived. The struts are required to support critical vertical loads from wing as well as lateral loads from waves and maneuvering. The structure can be reinforced at certain locations, such as joints between wing and strut and struts themselves (as shown in Fig. 3.21), where higher strength is required. The reinforcements are the most efficient way to reduce the number of struts, which can be accomplished by enlarging foil chords and/or extending the foil's span along the wing or struts. The reinforcements do not have significant impact to the ship's performance due to their small spans.
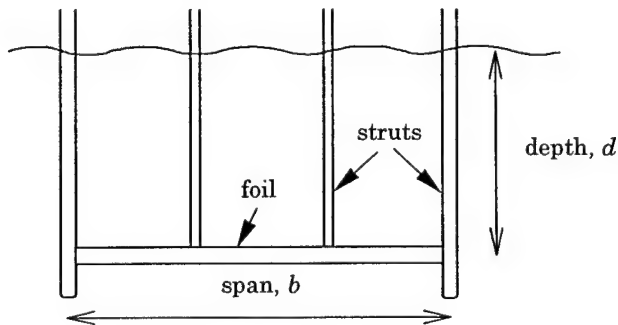
Fig. 3.20. Multi-bay foil-strut assembly.

28
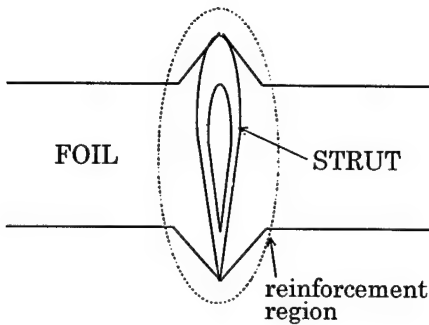
Fig. 3.21. Reinforcement at foil-strut joint.

The complex configuration of the wing-strut assembly prevents us from conducting the structural analysis manually. It is convenient and accurate to perform the analysis with a reliable finite element(FE) computer program. In this project, the structural optimization tool ADOP, Aeroelastic Design Optimization Program developed for aircraft wing design and optimization, is adopted for the purpose.

ADOP was developed for efficient static, dynamic, and aeroelastic analysis and optimization of large structural finite element models. The program analyzes structures composed of different finite elements including axial bar, bending beam, quadrilateral and triangular plane stress and plate-shell elements, elastic spring, solid element, lumped mass element, shear panel, and composite elements. Rigid connection elements, a general stiffness element (GENEL) and multiple point constraints (MPC) are also available for the modeling flexibility. Different loading conditions, including point, pressure, thermal, inertia, and any combination of them, can be included in static analysis. Linear buckling analysis for specified or all load conditions can be performed. In ADOP, dynamic analysis capabilities include modal, transient response, frequency response and flutter analyses. In the optimization, the program sizes structures to achieve a minimum weight while satisfying structural performance requirements such as stress, strain, displacement, modal frequency, buckling load, damage tolerance and flutter.

In the preliminary design, structural analysis focuses on determining design parameters including foil dimensions of wing and strut and number of struts. It will be very time-consuming if the structure is modeled in details, such as using plate-shell elements for

foil skins, defining spars and ribs with shear-panels, and tapering skin and panel thicknesses. In addition, a finite element model must be re-generated whenever a design parameter is changed. In order to perform quick trade study of those parameters, the wing and struts are approximated by bending beam elements with section properties computed by a simplified geometry with a uniform skin thickness. The simplification retains important structural behaviors of the wing-strut assembly and provides reasonable data for the ship's performance evaluation.

Variations of the design parameters are limited by performance. For example, the thickness to chord (t/c) ratio can not exceed certain limit to avoid cavitation during ship maneuvering. The wing area, i.e., the product of chord and span, is determined by the specified weight of the ship, the lift coefficient and a pre-selected water depth. Therefore, for a specific water depth and wing area only parameters like foil chord and number of struts can be varied. In this report, we have performed numerous finite element structural analysis by varying foil chord, foil span and number of struts in order to select a design that provides the best performance (L/D ratio) of the ship.

3.4.1 Finite Element Modeling

Finite element modeling of the wing and strut assembly starts with information of foil dimensions, i.e., chord and t/c, and wing span resulting from hydrodynamic analysis. Both wing and strut's foils are simplified by single cell box-type beams as shown in Fig. 3.22. The box-type structure is efficient for bending loads. The approximation however ignores the chordwise deformation of foils. The chord and t/c for wing and struts can be different. The real foil thickness is not uniform and is tapered up from the tip ad tapered down to the trailing edge. In order to represent the foils with a rectangular box for structural analysis, the width of the beams is reasonably approximated by using 75% of chord length. The height of beams is chosen as 85% of the chord multiplied by the associated t/c ratio. The skin thickness of the box is chosen to be uniform with a magnitude not to exceed 50% of the beam height. The foils can also be modeled by multiple-celled boxes in structural analysis. It does not,

however, significantly improve in the preliminary design but introduces complications in the design process. Using a single-cell box minimizes the number of design parameters and therefore effort in selecting the optimal structural layout with a reasonable accuracy. The configuration of the FE model is shown in Fig. 3.23, which is composed of beam elements for both wing and struts. The small circles indicate the locations of nodal points and a beam element is assigned between two neighboring points. Multiple elements are used to model the wing span between struts and along each strut. A Y-shape connection between struts and ship bottom is used to increase the lateral-load resistance of the struts. Different cross-section properties are assigned to the model depending on the reinforcements and their locations. Although, the FE model is simple, each model requires approximately two hours to generate by hands. It is time-consuming when many models are needed in the configuration trade study. A computer program is therefore developed to expedite the modeling process. With the program, the first model can be accomplished in an hour and any derivative of the model due to changes of design parameters can be completed in a matter of minutes.
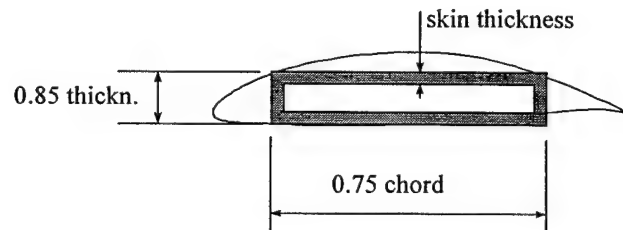
Fig. 3.22. Approximation of foil by a single-cell box for structural analysis.
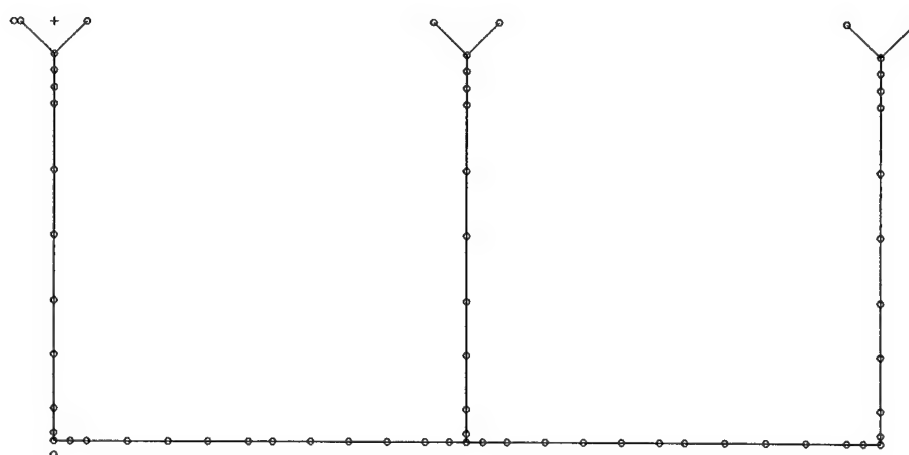
Fig. 3.23 Finite element model of wing-strut assembly

3.4.2 Load Distribution and Boundary Conditions

Only the strength design of the wing and strut assembly is considered in this study. Fatigue, damage tolerance and local buckling constraints, more properly considered in the detail design level, are not presently included. In detail design, any violation of these constraints can be corrected by increasing the skin thickness of foil or adjusting rib and spar locations inside the foil. The exterior of foil geometry remains unchanged. Therefore, the performance will not be affected by the correction.

There are three types of loads dominating the strength design: the vertical loads defined by the weight and payloads of the ship, lateral loads simulating a combination of critical side crushing waves and high speed turning of ship, and drag forces on foils. A safety factor of 200% is used for the vertical loads. The lateral loads are chosen to be 50% of the vertical loads and are modeled as concentrated forces applied to the struts at 60% of water depth. The drag forces with a 500% factor of safety are estimated based on foil geometry. The drag forces are applied at the same locations as the lateral loads but in the streamwise direction. A uniform distribution of vertical loads on the wing is assumed. The distributions of lateral loads and drag forces among struts are proportional to the amount of vertical loads carried by each individual strut. Fig. 3.24 show various loads applied to the wing-strut assembly.

A rigid connection of struts to the bottom of ship is assumed. Rigid joints are also assumed between wing and strut and between struts themselves. The finite element model is established along the centerline of wing and struts. A structural advantage that considers the finite dimensions of foils is not included in the analysis.
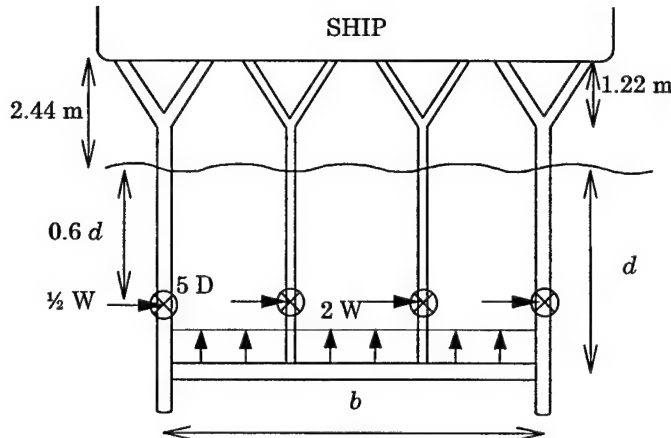
Fig. 3.24. Loads applied to the foil-strut assembly.

3.4.3 Structural Considerations

Structural design criteria include the bending strength of wing, combination of bending and axial strength of struts, and overall structural buckling of the wing and strut assembly. It is found that the overall buckling load is 30 times higher than the applied loads and is therefore not a design concern. The structural internal forces resulting from drag forces are also minor. The dominant design criteria are therefore the bending force on wing and combined bending and axial force on struts due to vertical and lateral loads. It is also found that the axial stresses in struts are only a small fraction (less than 5%) of maximum stresses. In order to efficiently conduct trade study of the wing and struts, bending forces are used as the safety index to adjust foil dimensions and spans of foils. Additional skin thickness will then be added to strut foils to account for axial forces.

Because the bending forces vary along wing spans and strut heights, it is advantageous to have various chord lengths on wing and struts to meet strength requirements. In other words, larger chords can be used at critical locations on wing and struts to avoid over-stress and smaller chords are used for under-stressed regions. This selection of chords requires evaluations of results from structural analysis, modification of the FE model and submission of a new computer run for the next analysis. The selection process is repeated until the bending strength everywhere on wing and struts are satisfied. The process is presently

conducted manually and requires approximately 16 hours to complete one wing study. Moreover, the final design is only considered acceptable but not optimal. It is to be hoped that an automated process including optimization be developed in the future, so that a wing design can be optimized in less than two hours.

Steel is selected for its high strength as the structural material. Different allowable stresses of steel were studied. A normal structural steel with an allowable stress of 249Mpa (36ksi) was used in the early analyses. However, this allowable resulted in a wing and strut assembly that cannot generate a satisfactory L/D ratio (see Sect. 5.1). Results presented in the following sections are based on steel with a higher allowable stress (380Mpa or 55ksi).

3.4.4 Structural Analysis

The study of a wing starts with a wing chord and the span of wing. A t/c ratio for wing foil and the water depth are also provided. Before a finite element model is generated, designer must select the number of struts, multiple wing and strut foils, and lengths of each foil. It is also assumed that the model has an equal bay between struts. The model is then generated by inputting the selected data into the modeling computer program developed for this contract. The program will output a bulk data filewhich contains the finite element model. Designer can visually check the model with a commercial graphical package such as PATRAN or IDEAS. If the model is appropriate, designer can submit a computer run using the analysis tool ADOP. In order to determine the distribution of lateral loads on struts, an initial ADOP run has to be performed with vertical loads only. 25% of the axial force carried by each individual strut is then chosen as the lateral load applied to the corresponding strut. The distributions of bending moments are different between cases with and without lateral loads as shown in Figs. 3.25 and 3.26. Fig. 3.25 shows the moment distribution on a three-strut wing for the case of vertical loads only. Fig. 3.26 includes the distribution on the same wing for both vertical and lateral loads. The two moment diagrams are quite different from each other. The inclusion of lateral loads has big impact to the strength of struts. It makes the moments at the joints between wing and strut and the moment at the Y joints critical. Since

the lateral loads can be applied from either side of the ship, the structure must be designed symmetrically with respect to its centerline.
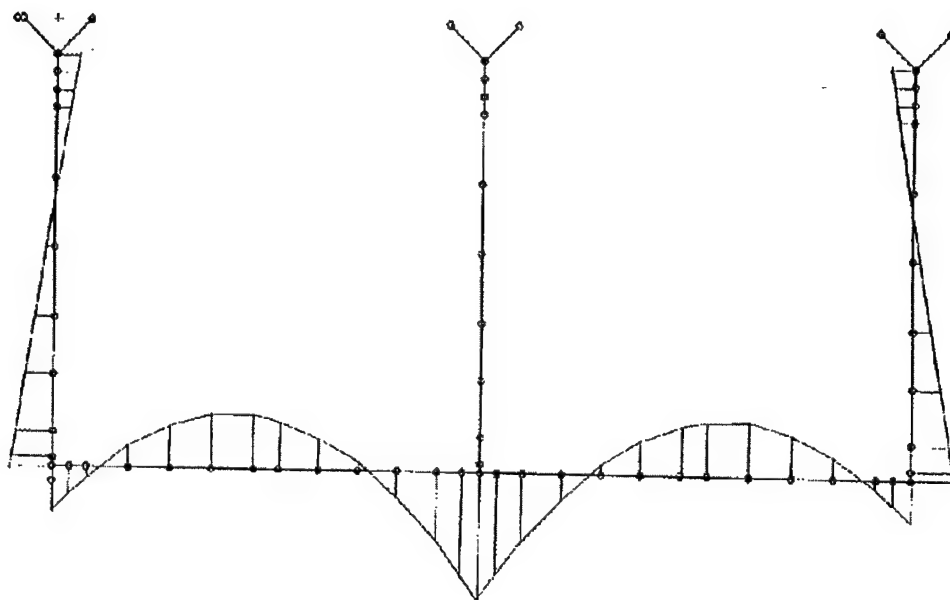
Fig. 3.25. Moment distribution due to vertical loads only.
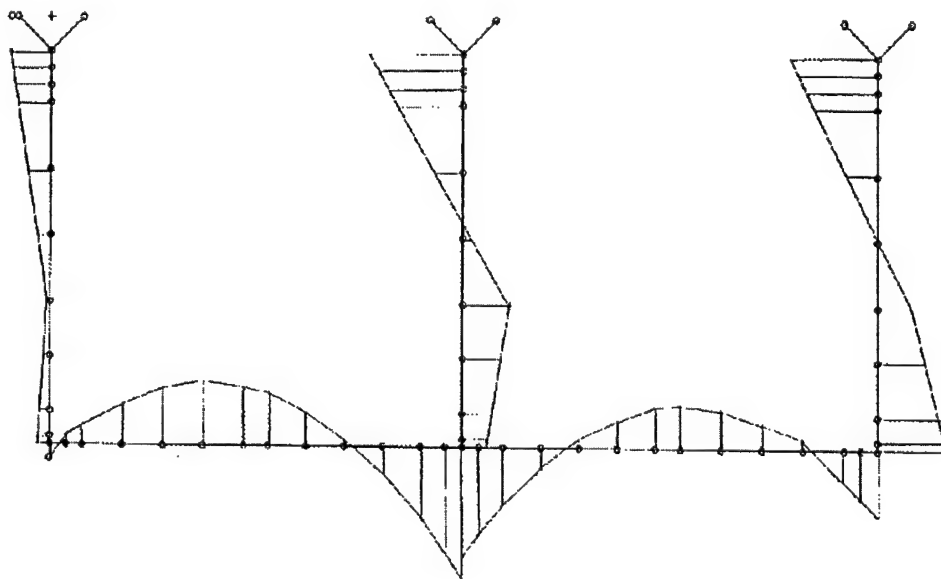
Fig. 3.26. Moment distribution due to both vertical and lateral loads

The computer output contains displacements of every nodal point and internal forces of beam elements. The internal forces include the axial force, twisting moment and two bending moments along principal axes of the beam cross-section. Because different chord lengths are used throughout the model, it is difficult for designer to visually check the bending moments of every beam element in the computer output and compare them with corresponding allowable moments in order to identify critical locations. To make the analysis easier, ADOP is modified to retrieve internal forces of beams with the same chord, compare the forces among the same group of beams and identify the most critical one in the group. In the analysis, all loads including vertical, lateral and drag are included.

Designer can check the maximum bending moment against the allowable, output by the modeling program, in the same group. If any allowable moment is smaller than the actual bending moment, the structure must be adjusted. There are several ways to achieve the purpose. Designer can either enlarge the chord of foil to gain sufficient bending strength, or adjust the span of the foil to redistribute the bending loads. If the adjustment is not satisfactory, an additional strut may need to be added to reduce the bending moment. Since the structure is indeterminate, the adjustment will somewhat alter the overall distribution of bending moments. It is difficult for designer to make a good initial selection of design parameters. Several trial-and-error computer runs are therefore needed.

A flow chart summarizing the structural design and evaluation procedure for the wing-strut assembly of fast ship is shown in Fig. 3.27.
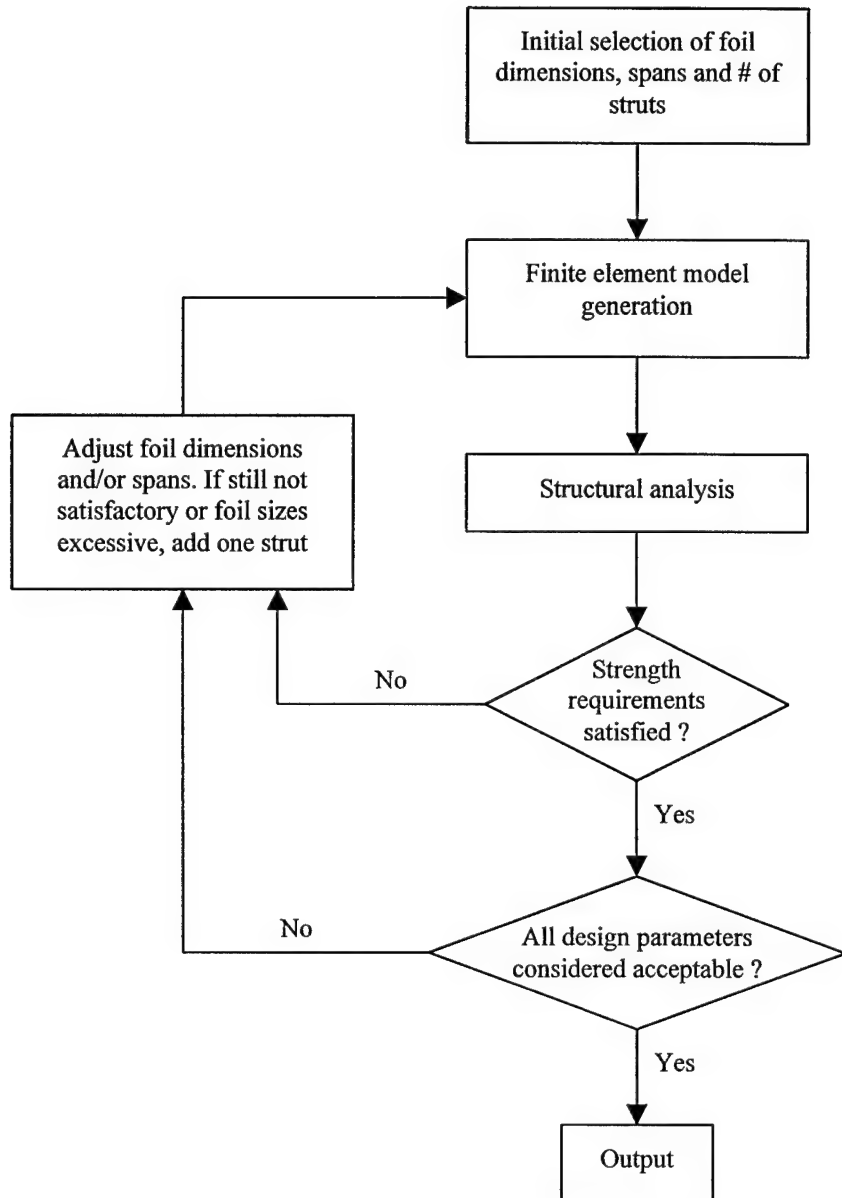
Fig. 3.27. Structural design process

3.4.5. Possible further studies

Because of limited time and manpower, the structural design and evaluation procedure developed herein, which is normally operated, can only lead to a reasonable but not optimal design. In order to obtain an optimal design, many more trade-offs among all design variables are required. If the procedure is not improved, the optimimal design requires approximately ten times more man-power and time to complete. The procedure can be improved by linking

the FE modeling program and ADOP together and by implementing optimization methods into the procedure. Therefore, when a basic wing is defined, the improved procedure will automatically generate a finite element model, perform structural analysis, compare maximum moment against allowable for each foil, compute sensitivities of each design parameter and modify all design parameters with a numerical search method. Several internal iterations in the procedure will be performed until an optimal design is achieved. It is expected that a complete design be accomplished in a few hours with minimum human involvement.

In this study, the structure of wing-strut assembly is simplified by bending beam elements. However, the real structure is made of spars, ribs and skin. They are welded or riveted together to form a multiple cell layout. Using beam elements cannot simulate the connections among skin, spars and ribs and is unable to predict the chordwise deformation as well as local stress concentration. Therefore, it is recommended that plate-shell elements, shear panels and even plane stress elements be used to model the wing-strut assembly for detailed analysis. For this type of structural models, instead of bending moment, the stresses should be used to monitor the safety of structures. In the detailed design optimization, more constraints such as stress, displacement, global and local buckling, fatigue and damage tolerance, and dynamic frequency can be included. The structural tool ADOP can still be used for this purpose. However, no geometrical parameters such as foil chords, spans and number of struts should be included at detail design level.

4.0 DESIGN APPROACH

This section presents the design approach implemented. It is designed to be suited for either parametric studies or to be incorporated in an optimization loop as shown in Fig. 4.1. The design is performed for *fixed speed and weight* (mass), i.e. the optimum design for that speed-weight combination is the one which provides the maximum L/D and is cavitation free, though it is likely to be right at the limit of cavitation.
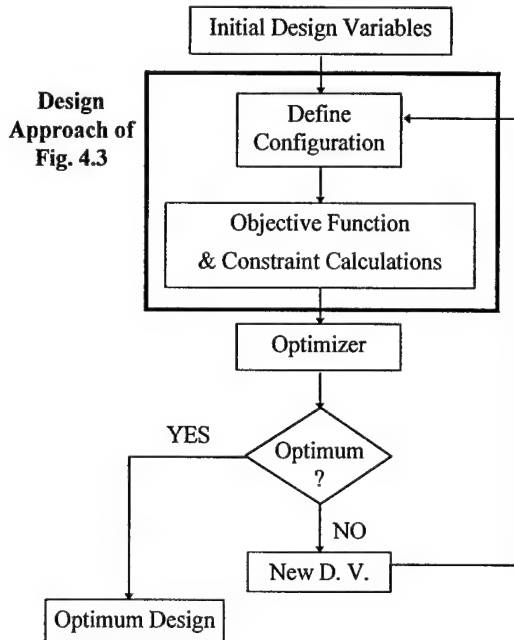
Fig. 4.1. Optimization loop

It might be worthwhile to note that, while the *maximum L/D for a given configuration* occurs when profile and induced drag coefficients are equal, since cavitation limits the achievable lift coefficient to low values, this maximum L/D, which we denote by $(L/D)_1$, might not be attainable. For the same configuration, let $(L/D)_2$ correspond to L/D at the cavitation limit. $(L/D)_1$ and $(L/D)_2$ are depicted on Fig. 4.2 on configuration B. For configuration A, $(L/D)_1 = (L/D)_2$. Also, as shown in Fig. 4.2, the *configuration leading to maximum feasible L/D* (configuration C) might not be operating at the maximum L/D for that configuration since cavitation prevents from reaching that lift coefficient.
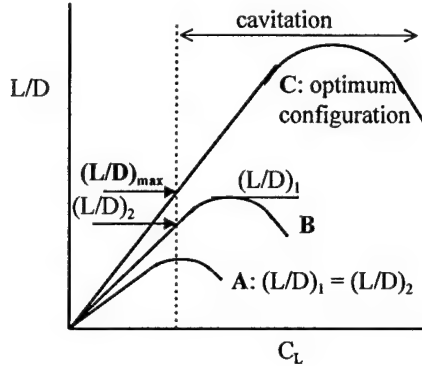
Fig. 4.2. Maximum L/D and cavitation

For fixed speed and weight, three *global* design variables can be identified:

- depth, d
- foil maximum thickness ratio, (t/c)
- aspect ratio, A

Other design variables exist, e.g. foil skin thickness for structural analysis, but are considered local since they can be adjusted independently of the rest. With these design variables, the procedure of Fig. 4.3 is used to generate the configuration and calculate its drag. As illustrated in Fig. 4.3, the tools presented in Sect. 3.0 play a key role in the design process. At the present time, they have not been implemented into a single computer program and the user needs to proceed step by step. The design process follows Fig. 4.3 and can be summarized as:

1. Given weight and speed, select a depth (first independent design variable). The cavitation index is then known. From foil cross-section optimization results of Sect. 3.2 for that cavitation index, select a feasible foil maximum thickness ratio (second independent design variable) such that the flow is cavitation free and obtain the corresponding section lift coefficient.

2. From typical three-dimensional flow calculations for strut-foil configurations (see Sect. 3.1), a corresponding three-dimensional lift coefficient can be determined. For all calculations reported here, it was assumed that the section lift coefficient of (1) could be obtained at all spanwise stations, and therefore, that $C_L = c_\ell$. If a rectangular planform is used, minor modifications to the foil cross-section of (1) have to be made near the strut-

foil junction. These modifications would have to be performed in the detailed design phase of the project.

3. The foil area can then be determined from

$$S = \frac{Mg}{\frac{1}{2}\rho V^2 C_L}$$

and selecting an aspect ratio $\left(A = b^2/S\right)$ enables to determine the chord and the span of the foil, assuming a rectangular planform, i.e. $S = b \times c$.

4. At this point, the lifting section of the configuration is entirely known. The induced drag can then be determined as described in Sect. 3.1, assuming that there are struts at the tips of the foil. Also, the chord Reynolds number, R_C, can be calculated and the foil profile drag coefficient is obtained from results of the CFD code of Sect. 3.2.

5. For preliminary calculations, an average strut maximum thickness ratio is determined based on the cavitation index at mid-depth, as described in Sect. 3.3.

6. A number of struts is selected. Their sizes (chord, skin thickness, etc.) are also chosen. A structural analysis is then performed as described in Sect. 3.4 to determine the maximum loads vs. the maximum allowables. The structure is then adjusted and subsequent structural analysis performed. This process is repeated until the strut area reaches a minimum while not exceeding the maximum allowables. This structural design process is described in Sect. 3.4 and enables to obtain the number of struts and their local chord.

7. The corresponding local Reynolds number can be determined at each strut cross-section and the profile drag results of Sect. 3.3 are integrated to obtain the profile drag coefficient of all struts.

8. The total drag coefficient is then obtained by adding induced drag and foil and strut profile drag:

$$C_D = C_{Di} + \varepsilon\left(C_{Df} + C_{Ds}\right)$$

where $\varepsilon = 1$ for the nominal drag coefficient, or $\varepsilon = 0.5,\ 0.25$ if skin friction reduction can be obtained. The resulting lift-to-drag ratio is then calculated along with the maximum (at the start of cruise) Break Horse Power (BHP) requirement which is given by

$$BHP = 6.7654 \frac{W_{\text{(metric tons)}} \, V_{\text{(knots)}}}{\eta_p \, L/D}$$

where $\eta_p = 0.75$.
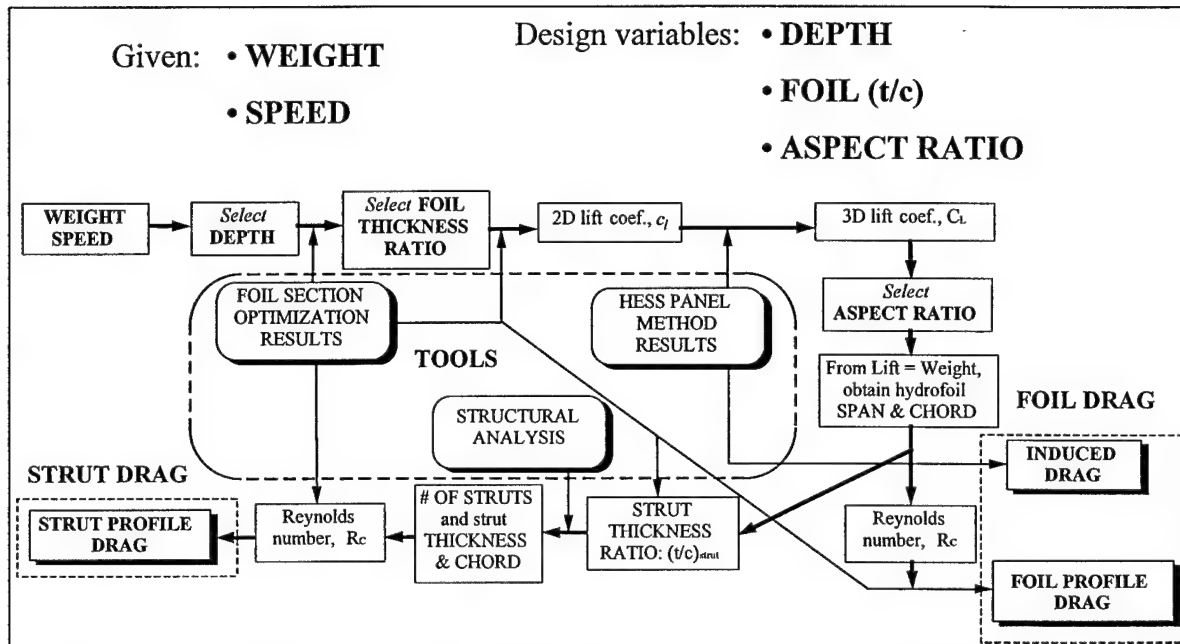
Fig. 4.3. Design approach

5.0 RESULTS FOR SINGLE FOIL CONFIGURATION

The approach of Sect. 4.0 using the tools of Sect. 3.0 is applied here to the single foil configuration shown in Fig. 5.1. Preliminary results are first presented and discussed in Sect. 5.1. Several improvements, such as structural reinforcements, use of end-plates, etc., are discussed in Sect. 5.2. The relevant improvements are then incorporated into the design process and results are shown for a variety of configurations in Sect. 5.3. Detailed results for a test case are also presented this section.
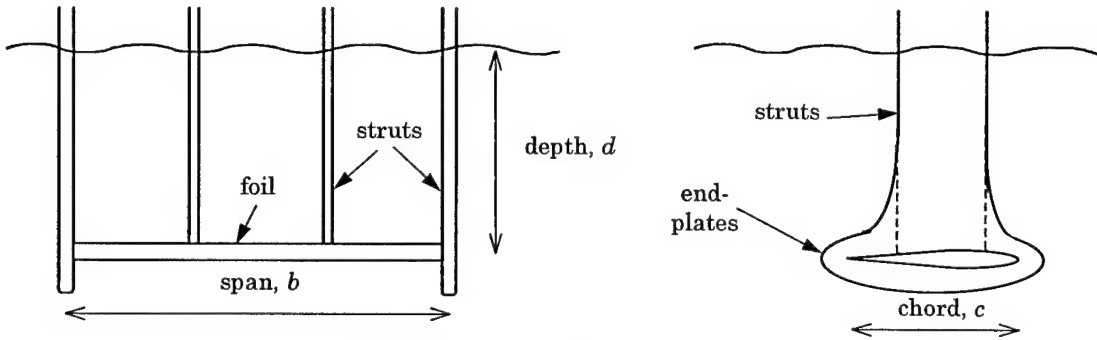
Fig. 5.1. Single foil configuration

5.1 Preliminary L/D results and key parameters

The design approach of Sect. 4.0 is applied here to the single foil configuration with a maximum stress allowable of 36 kpsi. Results are presented in Table 5.1 for 5000 tons at 60 and 75 knots. The independent design variables, the induced drag coefficient, the foil profile drag coefficient, the foil L/D at nominal skin friction coefficient, the strut profile drag coefficient normalized by the foil area, and the L/D at nominal, half and quarter skin friction coefficient are presented in bold characters. Calculations were performed for 2000 tons but are not reported here since the results were generally not as good. Only one test case was analyzed at 60 knots since greater interest exists in higher speeds. Compared with 75 knot test cases, however, the 60 knot case allows to obtain at least 50% greater lift-to-drag ratios. This difference is explained by the role cavitation plays on the maximum allowable foil thickness. At 60 knots and 10 m depth, a thickness ratio of 12% chord can be obtained without cavitation. To get the same lift coefficient and foil thickness ratio at 75 knots, the depth must

be increased to 20 m. In that case, however, the struts are so long that their number should be reduced by at least a factor of 2 in order to gain in L/D, provided the strut chord is unchanged.

The effect of an increase in aspect ratio in illustrated by comparing test cases P-2 and P-3. The number of struts required is increased from 7 to 9 and the corresponding strut drag is larger (0.0115 vs. 0.164). However, the induced drag coefficient is reduced from 0.0028 to 0.0018, which enables to obtain the same L/D (37 vs. 38) if quarter nominal skin friction can be obtained.

Also, it is worthwhile noting that, as illustrated in Fig. 5.2, the structural failures are in general due to two factors:

- in "shallow" water (10 m), the foil bending moment is critical, usually near the second strut;
- at higher depth (20 m), the strut root bending moment becomes critical due to the side load.

Fig. 5.2. Critical regions of the foil
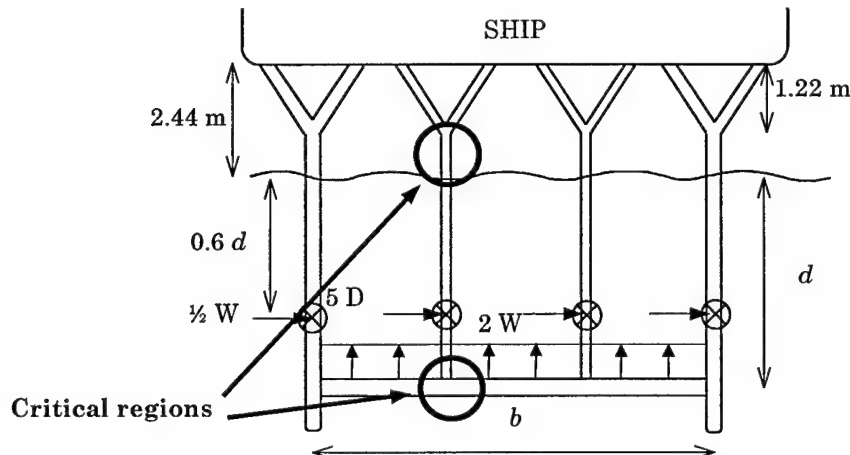
For this reason, interpolating or extrapolating the number of struts and their size to other test cases should not be considered reliable and the structural analysis should be performed for each given test case. This phenomenon also explains why the L/D results for test case P-4 are low: the gain in foil thickness has been outweighed by the strut length which causes large bending moments at the root of the struts.

Overall, however, these results are short of reaching a goal L/D of 50, even with skin friction reduction, and ways of improving the results should be investigated.

Test case #	P-1	P-2	P-3	P-4
M (tons)	5,000	5,000	5,000	5,000
V (kts)	60	75	75	75
d (m)	10	10	10	20
$(t/c)_{max}$	.12	.06	.06	.12
A	16	10	17	15
C_L	.41	.27	.27	.4
c (m)	3.96	4.93	3.78	3.31
b (m)	63.27	49.39	64.42	49.66
C_{Di}	.0043	.0028	.0018	.0033
$R_C \times 10^{-6}$	68	106	82	71
$C_{Df} (= c_{df})$	.0070	.0054	.0056	.0069
$(L/D)_{foil}$	36	33	37	39
$n_s, (c_s = c)$	7	9	16	13
c_{ds}	.0078	.0063	.0066	.0078
C_{Ds}	.0086	.0115	.0164	.0408
$(L/D)_{tot}$ @ c_f	21	14	11	8
BHP @ c_f	129 k	242 k	307 k	423 k
$(L/D)_{tot}$ @ .5 c_f	34	24	21	15
BHP@ .5 c_f	80 k	141 k	161 k	225 k
$(L/D)_t$ @ .25 c_f	50	38	37	26
BHP@ .25 c_f	54 k	89 k	91 k	130 k

Table 5.1. Preliminary L/D results for single foil configuration

5.2 Possible improvements

Three areas for possible improvements were investigated. The first one concerns structural reinforcements, the second one pertains to the use of foil sweep to increase the foil thickness, and the last one deals with the use of end-plates to further reduce induced drag.

Structural reinforcements

As previously mentioned, for depth around 10m, the critical section of the foil is usually located near the second strut, or for struts near the root. At these locations, the bending strength can be improved by increasing the thickness of the foil, which corresponds to increasing the foil chord locally. These structural reinforcements are shown in Fig. 5.3.
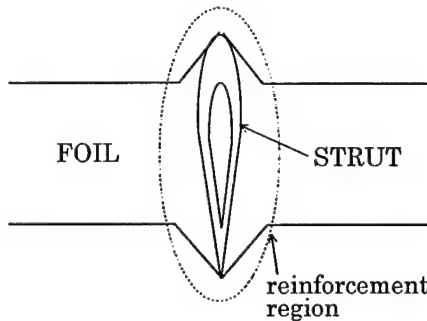
Fig. 5.3. Structural reinforcements

Max. Allowable	Reinforcement	# of struts	L/D improvement
36 kpsi	none	16	---
55 kpsi	none	13	14%
55 kpsi	yes	10	33%

Table 5.2. Effect of change in allowable and introduction of structural reinforcements.

Also, for preliminary calculations, a maximum allowable stress of 36 kpsi was used. As mentioned in Sect. 3.4, an allowable stress of 55 kpsi is justified. Table 5.2 shows the improvements which can be obtained by increasing the maximum allowable stress to 55 ksi, and adding structural reinforcements for the test case P-3. The increase in allowable gives a

14% improvement in L/D and adding structural reinforcements enables one to reach a 33% improvement.

Considering the large improvements observed, **structural reinforcements have been incorporated into the design process**. The drawback, however, is that they introduce additional structural design variables which need to be adjusted for optimum structural arrangement, thus requiring additional work.

Sweep for increased foil thickness

Sweep might be used to increase the cavitation onset speed of a wing, since sweeping decreases flow acceleration on the foil, thus increasing the pressure. Equivalently, for the same cavitation speed, i.e. minimum pressure, the foil can be swept and its thickness increased. This phenomenon is illustrated in Fig. 5.4 under infinite swept wing conditions, i.e. the three-dimensional flow does not vary in the spanwise direction. For a cavitation index of about 0.27, the foil maximum thickness ratio can be increased from 0.06 to 0.066 by sweeping at 30 deg., and to 0.075 by sweeping at 45 deg. This increase in foil thickness while generating the same lift coefficient may be beneficial for structural purposes.

When struts are added, since struts have to be streamlines, the advantage of sweeping might be lost. To investigate this matter, several test cases were analyzed. A strut-foil configuration with a rectangular planform and with the cross-section of the no-sweep case of Fig. 5.4 was generated. The configuration is at a depth of 10 m, has a chord of 3.78 m and a span of 64.4 m. A similar configuration was generated with the foil cross-section of the 30 deg.-sweep case of Fig. 5.4 and swept at 30 deg., and finally another configuration with sweep at 45 deg. using the 45 deg.-sweep cross-section of Fig. 5.4. For the present qualitative study, struts are added only at the tips. Fig. 5.5 shows the mid-chord pressure coefficient variation along the span to determine the areas of possible cavitation. The effect of the free surface seems to be less beneficial at mid-span with than without sweep. Also, the resulting lift coefficients vary slightly with sweep. Finally, the strut interference seems to be reduced for the most upstream tip ($y = 30$) and increased for the downstream tip ($y = -30$).
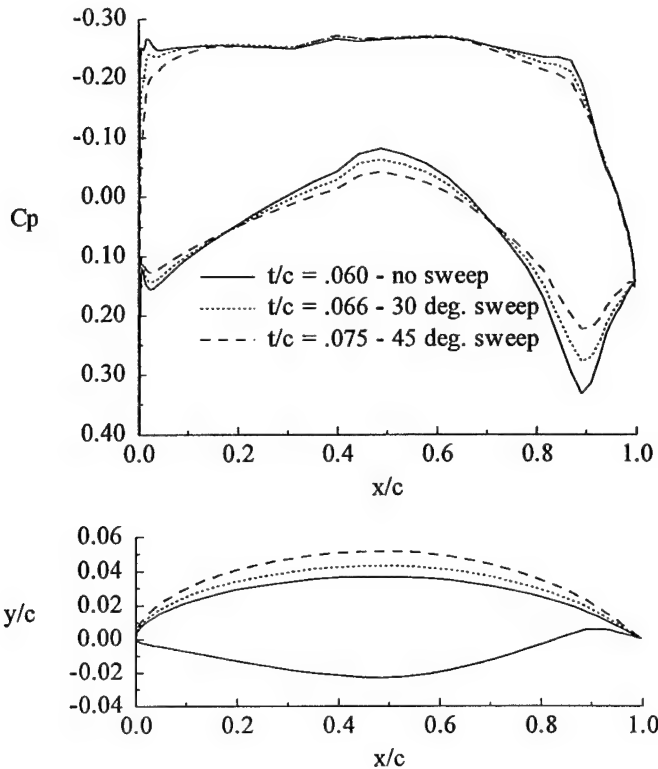
Fig. 5.4. Effect of sweep on foil thickness for a given minimum pressure coefficient.
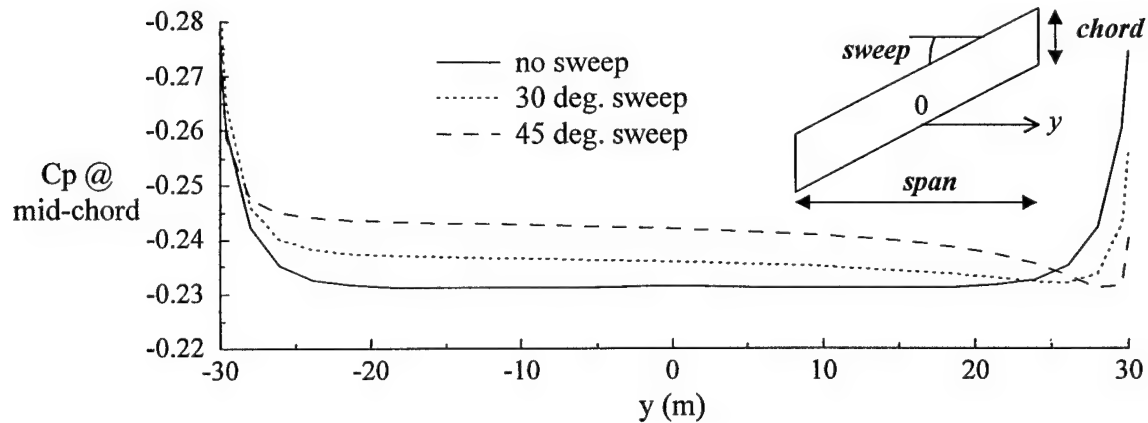
Fig. 5.5. Strut-foil interaction region and cavitation constraint.

To answer whether sweeping the foil might be beneficial while maintaining cavitation free flow in the strut-foil interaction region requires studying in detail the flowfield in that region and finding whether a feasible foil-strut shape exists for that purpose. Such a study is beyond the scope of the present preliminary design work and would require significant efforts.

If such a study demonstrated the possibility of designing a shape which would allow maintaining the larger foil thickness with sweep, a structural analysis would have to be

48

performed for the designed configuration to determine whether the bending strength of the system is increased, or equivalently, whether the number of struts required would be decreased.

Endplates for induced drag reduction

In all calculations presented thus far, end-struts of the same chord as the foil were used as means of reducing induced drag. Larger end-struts, or endplates, might be used to further reduce the induced drag. A test case was considered to evaluate the possible benefits of using end-plates for induced drag reduction. Fig. 5.6 defines the variables used to define the size of the end-plate. In all cases, the struts were extended all the way to the water surface, i.e. $h_1 = d$. The test case P-1 of the previous section is used as a base for comparison. Six test cases are considered. The term "small" is used to denote variables of the order of 0.1 c, and "large" is used for variables of the order of c. Changes in efficiency factor, e, are presented in Table 5.3. Improvements of the order of 10% in efficiency factor, corresponding to drag reductions of about 10%, can be reached by extending the plate downward, and downstream of the foil trailing edge. The larger endplates, however, would cause an increase in profile drag, thus leading to a smaller improvement, or possibly to an increase, in total drag.

In conclusion, endplates may be beneficial, but the improvement in total L/D will not be drastic. Their design should therefore be postponed to the detail design phase of the overall program.
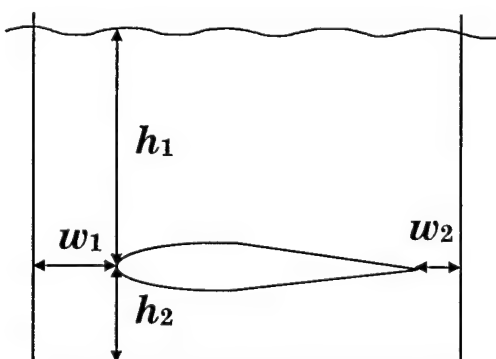

Fig. 5.6. Variables defining endplates

Configuration	% change in e
U-shaped end-strut	----
small endplate	-1.6
w_1 large	-11.8
w_2 large	+6.2
h_2 large	+10.2
all large	-2.6
w_2 and h_2 large	+13.6

Table 5.3. Changes in efficiency factor with size of endplate.

5.3 Final L/D results and discussion

Results with structural reinforcements and a maximum allowable stress of 55 kpsi are presented here for various points in the design space. Also, a modification in the foil design in the trailing edge region allowed to obtain slightly higher lift coefficients for the same foil thickness and the corresponding drag coefficient was adjusted to reflect these changes. Table 5.4 presents a summary of the calculations performed. For information, more detailed information is presented for the test case S-3 in Appendix 1.

Results are presented for 75 and 90 knots at depth of 10 or 13 m. High, moderate, and low aspect ratios are considered. The foil maximum thickness ratio is usually chosen so that a reasonable lift coefficient can be attained at the given cavitation index (which depends on speed and depth as described in Sect. 3.2).

Test case S-1 can be thought of as an initial design. S-2 shows the effect of increased aspect ratio, from 10 for S-1 to 17 for S-2. A gain in L/D can be obtained with quarter skin friction coefficient. S-3 corresponds to placing the foil slightly deeper (13 m instead of 10 m) which allows increasing the foil thickness ratio from t/c = 0.06 to 0.08 for the same lift coefficient (0.29). An increase in L/D is observed. Other calculations were performed for larger depths, but strut bending moments increased and became critical, thus not allowing reducing the number of struts. The corresponding L/D was naturally lower. Finally, S-6 presents a test case where the aspect ratio was drastically reduced to 4. The foil chord and its thickness are increased. The resulting foil has higher strength and the strut requirements are

therefore drastically reduced. The reduction in strut drag, however, is outweighed by the increase in induced drag.

When comparing results for 5000 tons at 75 kts and for the nominal skin friction coefficient, i.e. without skin friction reduction, L/D ratios are all very close to each other. Tradeoffs occur between strut profile drag and induced drag, i.e. a thicker wing (increased chord) comes to the expense of reduced aspect ratio. Foil profile drag remains essentially constant, its variations being due to Reynolds number variations. If skin friction drag reduction can be implemented, however, configurations with a greater aspect ratio will lead to better L/D, as is obvious when comparing S-3 (L/D = 51 with quarter skin friction coefficient) and S-6 (L/D = 32).

Test cases S-4, S-5, and S-7 correspond to design variable variations for 90 kts. Similar observations to 75 knot test cases can be made. At that speed, however, cavitation further reduces feasible foil thickness. Also, the dynamic pressure, which increases quadratically with speed, causes higher forces. The combination of both phenomenon explains why feasible L/D with quarter skin friction coefficient is reduced from 51 at 75 kts to 45 at 90 kts.

If the goal was to lift a total of 10000 tons, either two foils like S-3 would be required, or the size of the foil system could be increased. The two-foil system would, in general, cause an increase in induced drag which would reduce the overall L/D. In order to grasp what would occur if one were to lift 10,000 tons instead of 5,000 tons in a single foil, the foil span of test cases S-6 and S-7 was increased and test cases S-8 and S-9 were obtained. Due to the limit on the span at 65 m, the maximum aspect ratio achievable (approx. 8) does not reach as high values as for 5000 tons (approx. 17), and the resulting induced drag is larger, leading to a lower L/D ratio when skin friction drag reduction can be obtained.

Results presented in this chapter show that, with quarter skin friction drag reduction, an L/D greater than 50 can be obtained for 60 kts, the goal of L/D = 50 is achievable for 75 kts, and, for 90 kts, L/D ratios around 45 can be reached. The corresponding break horse power requirements for 10,000 tons are less than 100 khp, around 130 khp, and less than 200 khp, respectively.

CASE #	S-1	S-2	S-3	S-6	S-8	S-4	S-5	S-7	S-9
M (tons)	5000	5000	5000	5000	10000	5000	5000	5000	10000
V (kts)	75	75	75	75	75	90	90	90	90
d (m)	10	10	13	10	10	13	13	13	13
(t/c)	.06	.06	.08	.06	.06	.06	.06	.06	.06
AR	10	17	17	4	8	16	10	4	8
C_L	.290	.290	.292	.290	.290	.190	.190	.190	.190
c (m)	4.70	3.60	3.59	7.43	7.43	3.82	4.835	7.645	7.645
b (m)	46.97	61.24	61.08	29.71	59.42	61.16	48.35	30.58	61.16
C_{Di}	.0033	.0021	.0020	.0068	.0045	.0009	.0013	.0027	.0018
C_{Df}	.0053	.0055	.0059	.0050	.0050	.0053	.0051	.0048	.0048
$(L/D)_{foil}$	34	38	37	25	30	31	29	25	29
$<t/c>_s$	.080	.080	.088	.080	.080	.063	.063	.063	.063
n_s	6	10	7	3	4	8	5	3	5
C_{Ds}	.0073	.00965	.00905	.0045	.0036	.0091	.0070	.0059	.0051
$(L/D)_{tot}$ @ c_f	18	17	17	18	22	12	14	14	16
BHP @ c_f	188	199	199	188	308	338	290	290	507
$(L/D)_{tot}$ @ .5	30	30	31	25	33	24	26	24	28
BHP@ .5	113	113	109	135	205	169	156	169	290
$(L/D)_t$ @ .25	45	49	51	32	44	42	44	35	44
BHP@ .25	75	69	66	106	154	94	92	116	185

Table 5.4. Final L/D ratios for the single foil configuration.

6.0 RESULTS FOR BIPLANE CONFIGURATION

The three components of total drag are shown in Fig. 4.3 and are (1) configuration induced drag, (2) foil profile drag, and (3) strut profile drag. Induced drag is due to lift and can be reduced mainly by increasing aspect ratio. Foil profile drag is mainly due to foil skin friction drag, which greatly depends on foil area, thus on lift coefficient. Since cavitation limits the range of feasible lift coefficients, the only avenue for drastically reducing total drag from the levels observed for the single foil configuration would be to find means of reducing the number of struts, or more generally, reducing the strut wetted area. For this purpose, a biplane arrangement, which as a whole should allow for improved structural integrity, was investigated. The biplane configuration is shown in Fig. 6.1 and results are presented in this chapter. First, before L/D calculations could be carried out, both hydrodynamic and structural models had to be modified. These modifications are presented in Sect. 6.1 and 6.2, respectively. Sect. 6.3 presents the corresponding L/D results for two configurations.
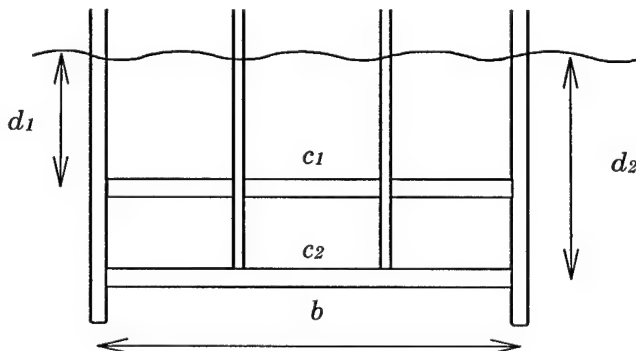
Fig. 6.1. Biplane configuration

6.1 Hydrodynamic interactions

Results of foil design/optimization shown in Sect. 3.2 correspond to a single foil without any interaction, either from other foils or from the free surface. For the depth to chord ratios considered, the effect of the free surface on the pressure distribution on a single foil are slightly beneficial. The same pressure distribution, i.e. same lift coefficient, can be obtained for a slightly thicker foil with free surface modeled than without the free surface, the difference being small. This difference was neglected in the calculations of Sect. 5.0.

When two foils are placed "close" to each other, they interact and the modifications in pressure distributions might need to be accounted for. Fig. 6.2 shows this interaction between two foils placed one chord apart on top of each other. This case would corresponds to a case at 75 kts when the foil chords would both be about 4 m, the first foil would be placed at 9 m depth, and the second one at 13 m. For simplicity, the effect of the free surface was not accounted for in the results presented here and all calculations are two-dimensional. For the test cases presented in Sect. 6.3, however, three-dimensional effects and free surface are taken into account.

Fig. 6.2a presents results for the upper foil, and Fig. 6.2b shows the results for the lower foil. Without any interaction, i.e. each foil is by itself, thickness ratios of 0.073 and 0.07 could be used for the upper and lower foils, respectively, while maintaining cavitation free flow. The corresponding pressure distributions are shown in Fig. 6.2 with continuous lines. Even if, as reflected in Fig. 6.2 (lower maximum negative pressure for the upper foil), the cavitation index for the upper foil is smaller than for the lower foil, a thicker upper foil was feasible at the cost of a reduced lift coefficient. This value was selected to have two foils of about the same thickness (without interaction). As discussed in Sect. 3.2, the pressure distribution clearly shows that the thickness ratio of the lower foil would be in the middle of the feasible thickness range (thickness can be increased by fattening the lower surface while not reaching the cavitation limit). The upper foil, however, operates near the maximum cavitation free thickness (a rather small fattening of the lower surface would cause cavitation on the lower surface).

The dashed lines represent the computed pressure distributions when the two foils which, without interaction, lead to the proper pressure distribution (i.e. cavitation free while maximizing lift coefficient) are placed a chord apart in a biplane arrangement. It is seen that drastic changes in pressure distribution occur on the upper foil which would lead to cavitation on both upper and lower surfaces of the upper foil. Changes in the lower foil are less drastic and are actually favorable.

The dotted lines present the results after modification of the foil shapes (also shown in dotted lines and compared with the original foil in continuous lines) in order to obtain cavitation free flow with biplane interaction. The necessary modifications lead to a thinner upper foil (t/c = 0.06 instead of 0.073) which also generates less lift (lower surface velocities

are increased due to the lower foil beneath it) and to a slightly thicker lower foil (t/c = 0.08 instead of 0.07), its lift coefficient being essentially unchanged. The consequences of the interaction are of primary importance for the upper foil since its thickness tends to drive the number of struts required for structural considerations.

This interaction is taken into account in the results presented in Sect. 6.3, along with the effect of the free surface on pressure distribution. Also, the induced drag calculation is performed for each test case using the Hess panel method for the modified configuration, in contrast with Sect. 5.0 where all results for induced drag are derived from Fig. 3.12.


(a)

(b)
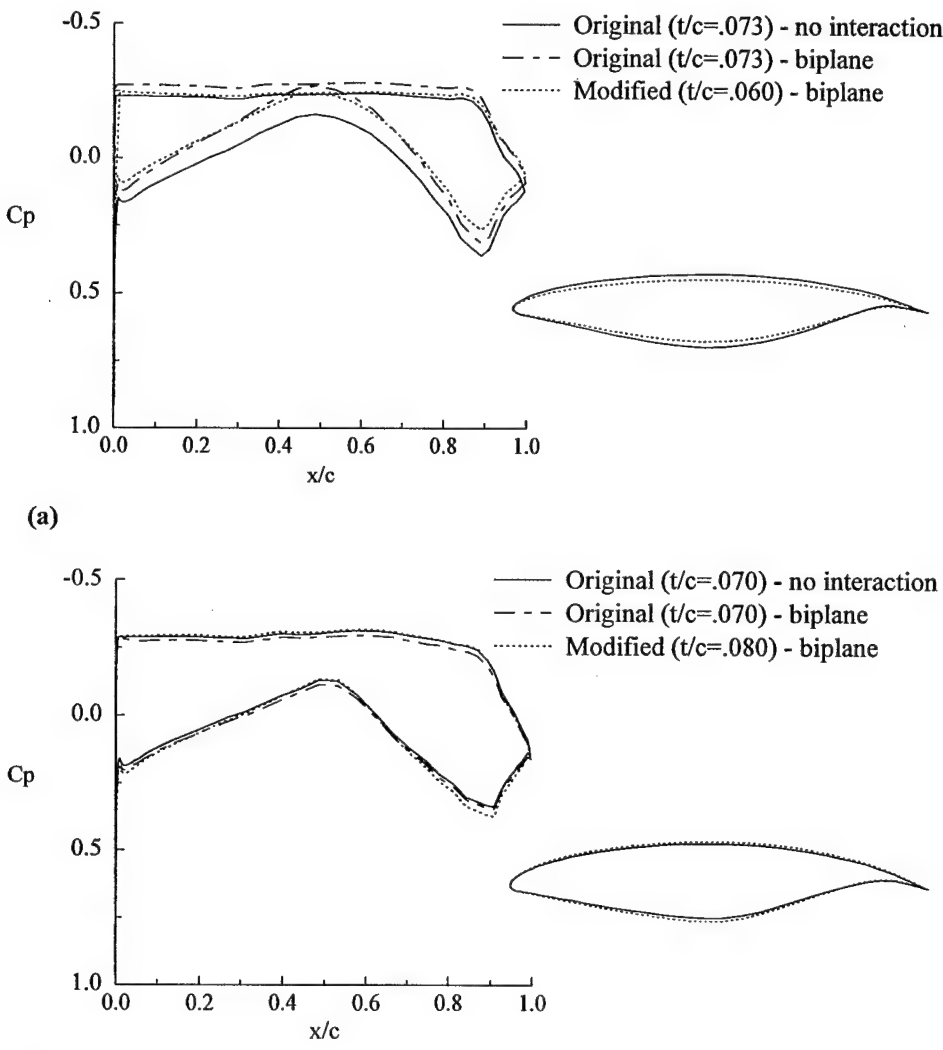
Fig. 6.2. Interaction between two foils in a biplane arrangement placed a chord apart; (a) upper foil and (b) lower foil.

6.2 Modifications in structural analysis

For the single foil configuration, the side load was centered at 60 % depth on the struts. Since the biplane has to foil depths, this procedure had to be modified accordingly. The side loads applied to the biplane configuration are presented in Fig. 6.3. Δ_1 and Δ_2 are determined to satisfy the force and moment conservation equations. The continuous load is replaced by two point loads in the model, W_1 and W_2, placed at 2/3 Δ_1 and ½ Δ_2 as shown in Fig. 6.3. W_1 and W_2 correspond to the loads on the upper and lower foils, respectively.

The structural reinforcements discussed in Sect. 5.2 have also been included.
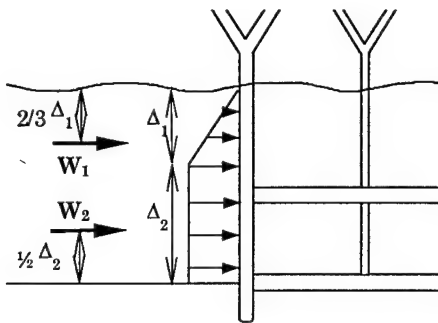
Fig. 6.3. Side load model for the biplane configuration.

6.3 L/D results

Table 6.1 presents results for two biplane configurations, one for 5000 tons and the other for 10000 tons, at 75 knots. The span of both upper and lower foils are the same, but their chord, constant for each foil, are allowed to be different. The depths considered are 9 m for the upper foil and 13 m for the lower foil. Results presented here take into account the interaction of the two foils and of the free surface.

For test case B-1, the thickness ratio of the upper foil is a lot less than for the lower foil because of the interaction and reduced cavitation index at the lesser depth. To compensate for the lower thickness ratio, a smaller aspect ratio for the upper foil is used, thus leading to a larger upper foil chord. This test case can be compared with test case S-1 of Sect. 5.3, even if deciding a proper test case for comparison is not straightforward. L/D results without skin friction reduction are of the same order as for the single foil. If quarter skin friction can be obtained, however, L/D results are less than for the single foil configuration, mainly due to a decrease in lift coefficient, other coefficients being almost constant. In particular, the strut

drag coefficient is almost unchanged: the benefits of the biplane structural arrangement are cancelled by the reduction in foil thickness.

The second test case (B-2) can be compared with test case S-8 and was investigated to determine how lifting 10000 tons with two foils compares with lifting 10000 tons in one foil taking advantage of all the span available (65m). The aspect ratio for the biplane configuration is higher leading to a slightly lower induced drag coefficient. However, since the foil thickness is smaller (shorter chord), the foil strength is reduced and the number of struts goes from 4 for S-8 to 10 for B-2. Interestingly, the resulting L/D with quarter skin friction drag remains unchanged (44 vs. 43).

In conclusion, from the test cases considered, even if the biplane configuration does not seem to be worse than the single foil configuration, it does not seem to offer significant advantages either. The benefits of the structural arrangement are traded for reduced foil thickness and therefore more struts leading to an increase in strut drag. A deeper investigation might be warranted.

Case #	B-1	B-2
M (tons)	5000	10000
V (kts)	75	75
d_1, d_2 (m)	9, 13	9, 13
$(t/c)_1$, $(t/c)_2$	.05, .09	.06, .08
AR_1, AR_2	10.7, 15.4	16, 16
C'_{L1}, C'_{L2}	.21, .29	.18, .33
C_L	.247	.255
c_1, c_2 (m)	3.80, 2.64	3.96, 3.96
b (m)	40.7	63.3
C_{Di}	.00293	.00296
C_{Df}	.00575	.0056
$(L/D)_{foil}$	28	30
$<t/c>_s$	.083	.083
n_s	7	10
C_{Ds}	.00693	.00605
$(L/D)_{tot}$ @ c_f	16	17
BHP @ c_f	211	398
$(L/D)_{tot}$ @ .5	27	29
BHP@ .5	125	233
$(L/D)_t$ @ .25	40	43
BHP@ .25	85	157

Table 6.1. L/D results for the biplane configuration.

7.0 CONCLUSION

This report presents a summary of the work accomplished at California State University, Long Beach under contract with the Office of Naval Research from July 1, 1997 to Jan. 31, 1998. The program overview is presented in Sect. 2.0.

The objective of the study was to determine the achievable lift-to-drag ratio (L/D) of an isolated foil-strut arrangement, hopefully larger than 50, at high transit speeds, possibly greater than 75 knots, while lifting masses of 5,000 or 10,000 tons.

The first phase of the program consisted of developing the tools necessary for the study. This phase, presented in Sect. 3.0, included (1) the introduction of a negative image option to the three-dimensional Hess higher-order panel method to model high Froude number free surface flows; (2) the development of a foil cross-section design/optimization method (which combines state of the art Computational Fluid Dynamics methods with optimizers); and (3) setting up a structural analysis based on the finite element method.

A design approach, shown in Sect. 4.0, was implemented using these tools. Given a set of design variables, the transit speed, and the mass to lift, the configuration and its drag are calculated following the procedure of Sect. 4. Design variables can then be varied to improve the design, i.e. reduce drag. The design approach is general, although time did not permit to implement it into a general optimization procedure, and was used for several types of configurations.

Results are presented in Sect. 5.0 for a single foil configuration. Preliminary results showed that modifications to the design needed to be made in order to reach L/D greater than 50. The effects of foil sweep to increase foil thickness, structural reinforcements to increase strength locally, and endplates to reduce induced drag were analyzed. Structural reinforcements showed great benefits and were incorporated in all subsequent designs. Several points in the design space were analyzed for speeds of 75 and 90 knots, and masses of 5000 and 10000 tons. Results showed a rather small dependency of the design parameters on L/D, suggesting that drastic improvements could not be obtained by conducting extensive parametric studies.

Therefore, a biplane configuration was investigated to determine whether a more sound structural arrangement could lead to substantial reductions in number of struts.

Preliminary results indicate that similar L/D results should be expected for this type of arrangement when comparing with the single foil configuration.

The results show that, with quarter skin friction drag reduction, an L/D greater than 50 can be obtained for 60 kts, the goal of L/D = 50 is achievable for 75 knots, and, for 90 knots, L/D ratios around 45 can be reached. The corresponding break horse power requirements for 10,000 tons are less than 100 khp, around 130 khp, and less than 200 khp, respectively. These values are less than the limit of 200 khp set forth by DARPA. Several avenues could be investigated to further reduce drag. As previously discussed, the design process exposed therein could be implemented automatically and incorporated into an optimization loop. Also, other types of structural arrangements could be analyzed in order to minimize the strut wetted area.

REFERENCES

1. J. L. Hess and A.M.O. Smith, Calculation of nonlifting potential flow about arbitrary three-dimensional bodies, *Journal of Ship Research,* 8, No. 2, 22 (September 1964).

2. J. L. Hess, The problem of three-dimensional lifting flow and its solution by means of surface singularity distribution. *Comp. Meth. in Appl. Mech. and Eng.*, Vol 4, 1974; also McDonnell Douglas Report No. MDC J5679, 1972.

3. J. L. Hess, D.M. Firedman and R.W. Clark, Calculation of compressible flow about three-dimensional inlets with auxiliary inlets, slats and vanes by means of a panel method. McDonnell Douglas Report No. MDC J3789, 1985; also NASA CR-174975 and AIAA Paper No. AIAA-85-1196.

4. Vanderplaats, Miura & Associates, Inc., "DOT Users Manual, Version 4.10," VMA Engineering, ©1994.

5. R. Hicks and P. Henne, "Wing Design by Numerical Optimization," *J. Aircraft*, Vol. 15, No. 7, pp. 407-413, July 1978.

6. Eyi S., "Performance Evaluation and Improvements of CFD-based Aerodynamic Design Optimization", Ph.D. Dissertation, University of Illinois, Urbana Champaign, 1995.

7. T. Cebeci, E. Besnard and H.H. Chen, "Calculation of Multi-element Airfoil Flows, Including Flap Wells," AIAA Paper No. 96-0056, Jan. 1996.

8. T. Cebeci, *An Engineering Approach to the Calculation of Aerodynamic Flows*, to be published, 1997.

9. T. Cebeci and K.C. Chang, "An Improved Cebeci-Smith Turbulence Model for Boundary-Layer and Navier-Stokes Methods," *Proceedings of the 20th ICAS/AIAA Aircraft System Conference*, Sept. 1996.

10. Squire, H.B., and Young, A. D., *The calculation of the profile drag of aerofoils*, ARC RM 1838 (1938).

11. E. Besnard, A. Schmitz, E. Boscher, N. Garcia, and T. Cebeci, " Two-Dimensional Aircraft High Lift System Design and Optimization," Paper No. 98-0123, Jan. 1998.

12. Abbott, I.H. and Von Doenhoff, A.E. *Theory of Wing Sections,* Dover Publications, Inc., NY, 1959.

APPENDIX

Based on test case S-3

1. LIFT-TO-DRAG RATIOS
Values for nominal, half, and quarter skin friction coefficient
1.1 Complete assembly
L/D = 17, 31, 51
1.2 Foil alone
L/D = 37, 59, 84

2. FOIL DATA
2.1 Depth (in meters)
d = 13 m
2.2 Induced drag for foil-strut system
2.2.1 Coefficient
$C_{Di} = 0.0020$
2.2.2 Absolute value (in Newton)
$D_i = \frac{1}{2}\rho V^2 S C_{Di} = 336,225.14N$
2.3 Geometry (in meter)
2.3.1 Chord (multiple values if tapered along the span)
See Table A.1 and Fig. A.1
2.3.2 Span
b = 61.08 m
2.3.3 Thickness (multiple values if tapered along the span)
See Table A.1 and Fig. A.1
2.4 Drag
2.4.1 Schoenherr coefficient magnitude

Defined by: $\quad \dfrac{1}{\sqrt{C_f}} = 4.13\log_{10}(R_c C_f)$

$C_f = 0.002097$ (2D flat plate)

2.4.2 Full profile drag coefficient (friction plus form)
Calculated by CFD code: $C_{Df} = 0.0059$
2.4.3 Full profile drag absolute value (in Newton)
$D_f = \frac{1}{2}\rho V^2 S C_{Df} = 991,864.17N$
2.5 Spanwise load distribution (in Newton per meter)
See Fig. A.2
2.6 Critical structural load data
2.6.1 Location(s)
2.6.2 Stress values(in MPa)
2.6.3 Shear force (in Newton) -not reported because not critical-
2.6.4 Bending moment (in Newton-meter)
2.6.5 Section modulus (in meter cubed)

See Table A.1

3. STRUT DATA

3.1 Number

$n_s = 7$

3.2 Geometry below waterline

3.2.1 Length (foil to waterline)

$d = 13$ m

3.2.2 Chord (multiple values if tapered)

See Table A.1 and Fig. A.1

3.2.3 Thickness (multiple values if tapered)

See Table A.1 and Fig. A.1

3.3 Geometry above waterline

See Fig. A.1

3.4 Top and bottom boundary conditions

All joints are considered rigid.

3.5 Drag

3.5.1 Schoenherr coefficient magnitude

$C_f = 0.002097$ (2D flat plate)

3.5.2 Full profile drag coefficient (friction plus form)

Calculated by CFD code: $C_{Ds} = 0.00905$

3.5.3 Full profile drag absolute value (in Newton)

$D = \frac{1}{2}\rho S V^2 C_{Ds} = 1,521,418.8$N

3.6 Load distribution

3.6.1 Spanwise distribution for 0.5g side load (in Newton per meter)

See Fig. A.2

3.6.2 Load distribution from carryover onto the strut of the foil's bound circulation

See Fig. A.3

3.6.3 Vertical load at bottom (from foil)

See Fig. A.2

3.7 Critical structural load data

3.7.1 Location(s)

3.7.2 Stress values (in MPa)

3.7.3 Shear force (in Newton) -not reported because not critical-

3.7.4 Bending moment (in Newton-meter)

3.7.5 Section modulus (in meter cubed)

See Table A.1

|	Chord	Thickness ratio	Section Modulus	Max. Bending Moment	Max. Bending Stress	Allowable Bending Moment
W1	3.59 m	0.08	0.026745 m^3	1.0159E7 Nm	379.85 MPa	1.0142E7 Nm
W2	4.16 m	0.08	0.041738 m^3	1.5375E7 Nm	368.37 MPa	1.5827E7 Nm
W3	4.52 m	0.08	0.053382 m^3	1.9725E7 Nm	369.51 Mpa	2.0242E7 Nm
W4	4.83 m	0.08	0.064769 m^3	2.4381E7 Nm	376.43 Mpa	2.4562E7 Nm
S1	3.59 m	0.088	0.032355 m^3	1.2247E7 Nm	378.52 Mpa	1.2270E7 Nm
S2	4.47 m	0.088	0.062228 m^3	2.2759E7 Nm	365.74 MPa	2.3597E7 Nm
S3	4.62 m	0.088	0.068643 m^3	2.5353E7Nm	369.34 MPa	2.6030E7 Nm
S4	4.78 m	0.088	0.075428 m^3	2.7948E7 Nm	370.52 MPa	2.8603E7 Nm

Table A.1- Structural results obtained for test case S-3
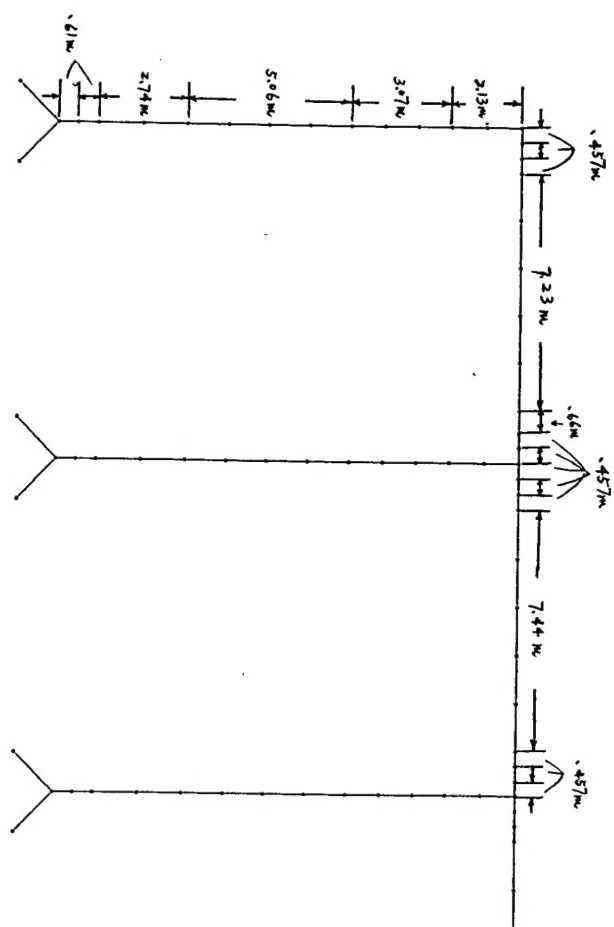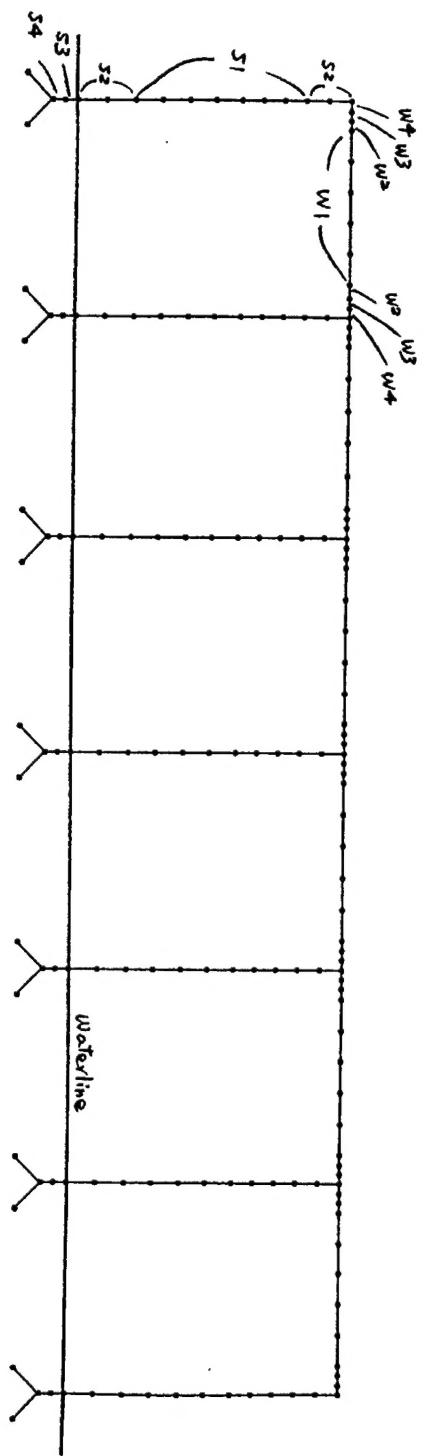
Fig. A.1 - Finite element model

A4
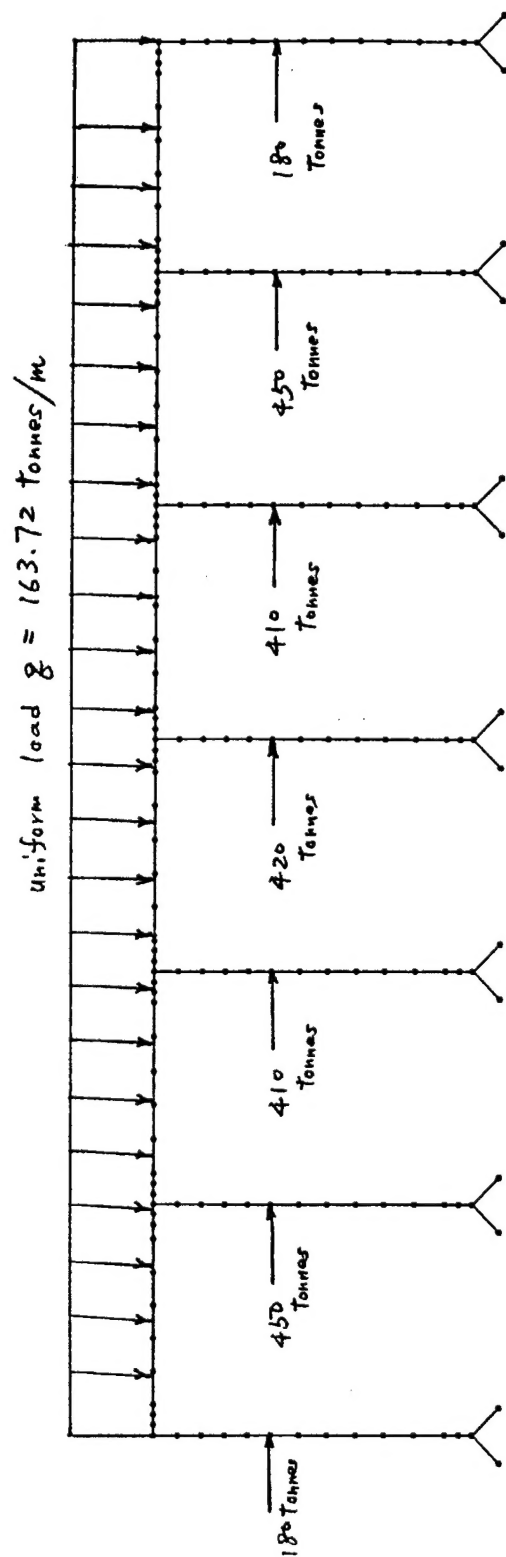
Fig. A.2 - Location of forces on finite element model
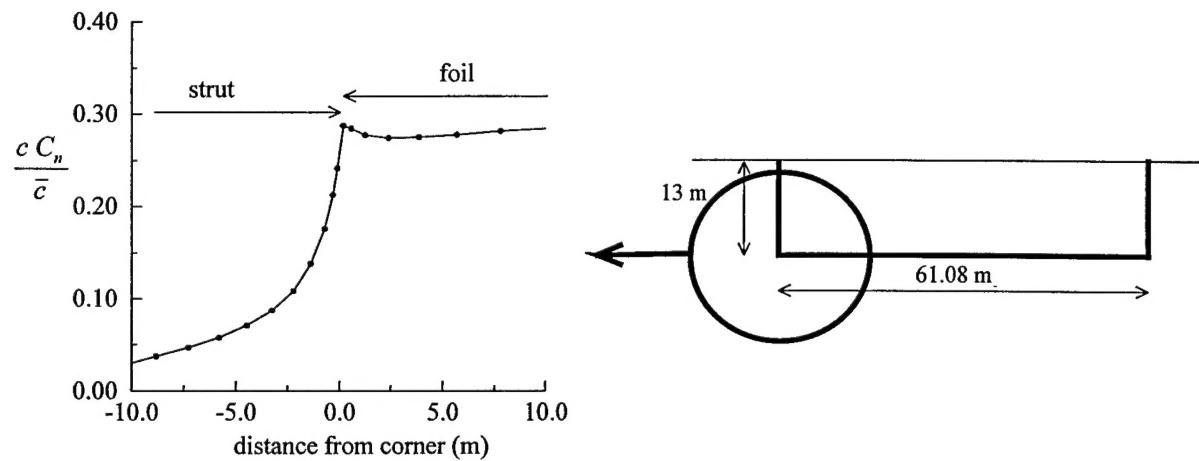
Fig. A.3 - Circulation distribution at the strut-foil junction